National Science Review Advance Access published December 21, 2013

REVIEW

National Science Review
00: 1–29, 2013
doi: 10.1093/nsr/nwt002
Advance access publication 0 0000

PHYSICS

Piezotronics and piezo-phototronics—fundamentals and applications

Zhong Lin Wang[1,2,*,†] and Wenzhuo Wu[1,†]

ABSTRACT

Technology advancement that can provide new solutions and enable augmented capabilities to complementary metal–oxide–semiconductor (CMOS)-based technology, such as active and adaptive interaction between machine and human/ambient, is highly desired. Piezotronic nanodevices and integrated systems exhibit potential in achieving these application goals. Utilizing the *gating* effect of piezopotential over carrier behaviors in piezoelectric semiconductor materials under externally applied deformation, the piezoelectric and semiconducting properties together with optoelectronic excitation processes can be coupled in these materials for the investigation of novel fundamental physics and the implementation of unprecedented applications. Piezopotential is created by the strain-induced ionic polarization in the piezoelectric semiconducting crystal. Piezotronics deal with the devices fabricated using the piezopotential as a 'gate' voltage to tune/control charge-carrier transport across the metal–semiconductor contact or the p–n junction. Piezo-phototronics is to use the piezopotential for controlling the carrier generation, transport, separation and/or recombination for improving the performance of optoelectronic devices. This review intends to provide an overview of the rapid progress in the emerging fields of piezotronics and piezo-phototronics. The concepts and results presented in this review show promises for implementing novel nano-electromechanical devices and integrating with micro/nano-electromechanical system technology to achieve augmented functionalities to the state-of-the-art CMOS technology that may find applications in the human–machine interfacing, active flexible/stretchable electronics, sensing, energy harvesting, biomedical diagnosis/therapy, and prosthetics.

Keywords: piezotronic effect, piezo-phototronic effect, piezopotential, piezotronics, MEMS, sensors

[1]School of Materials Science and Engineering, Georgia Institute of Technology, Atlanta, GA 30332-0245, USA and [2]Beijing Institute of Nanoenergy and Nanosystems, Chinese Academy of Sciences, Beijing 100083, China

[†]These authors contributed equally to this work.

***Corresponding author**. E-mail: zlwang@gatech.edu

Received 22 July 2013;
Revised 25 August 2013;
Accepted 25 August 2013

INTRODUCTION

In addition to the technology trajectory of miniaturizing components for enhanced performance as per Moore's law, which has been the dominating roadmap that drives the advancement of information technology in the last few decades, much effort has been paid on integrating individual micro/nanodevices with diversified functionalities into multi-functional micro/nano-systems (MNS) and large-scale networks for structural health and environmental monitoring, personal electronics, human–machine interfacing and biomedical diagnosis/therapy [1–6]. Integration of these discrete devices with dedicated functionality toward self-powered smart systems, which incorporate the embedded energy scavenging/storage units for perpetual and maintenance-free operations, is proposed to be one of the major roadmaps for electronics [7–9]. The miniaturized dimensions of nanomaterials and the capability of modulating their compositions/properties in well-controlled manners not only present the potential for addressing some of the critical challenges faced by silicon-based microelectronics, but also enable the possibility of incorporating into systems with diversified functionalities, which do not necessarily scale as per Moore's law to complement digital signal/data processing with augmented functional capabilities, such as interactions between machine and human/environment (Fig. 1). Approaches for developing a direct interface between the machine and human/ambient are highly desired for realizing the above applications.

Vibration-based mechanical signals are ubiquitous in the environment and provide abundant

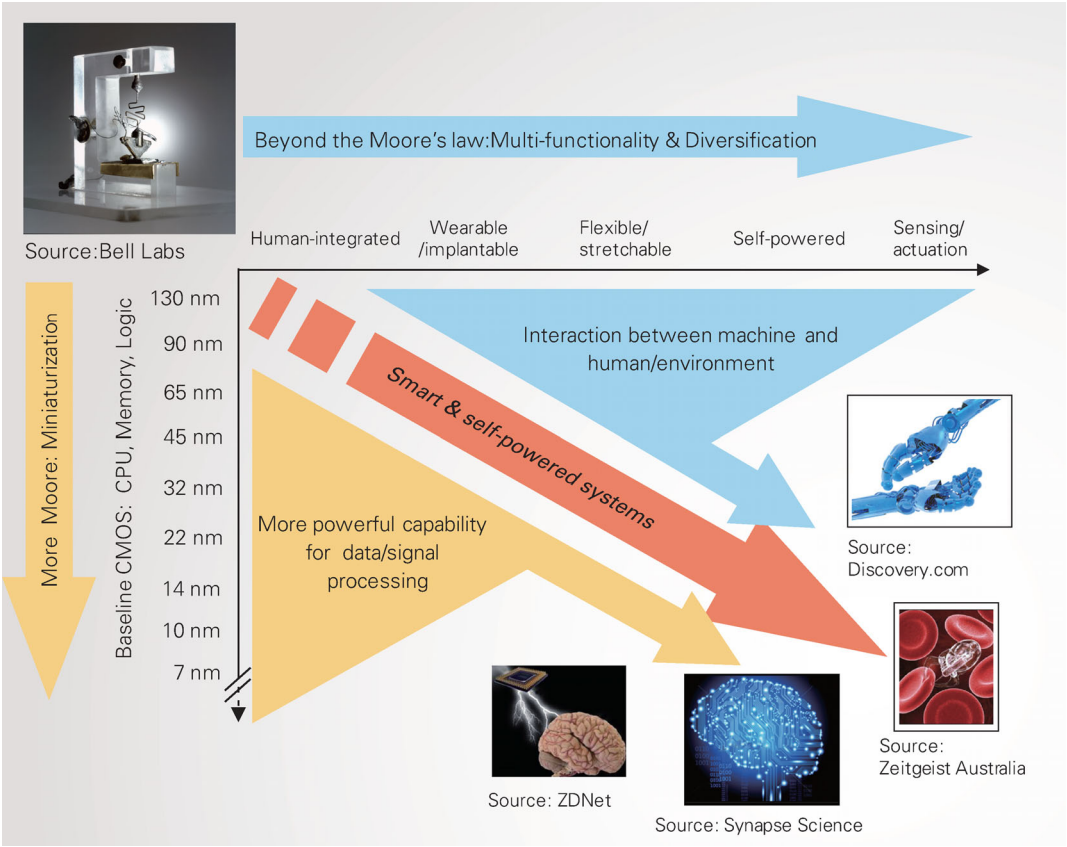

Figure 1. Perspective of electronics technology beyond Moore's law. The vertical axis represents the miniaturization of device dimension and the increase of integrated device density for more powerful data/signal processing. The horizontal axis represents the diversification and integration of device functionality for novel applications, such as wearable/implantable human-integrated electronics and self-powered technology for sensing and actuation. The future of electronics is an integration of more powerful data processing and more integrated functionalities. Adapted from [10].

actuation sources for potentially controlling the electronics in the MNS [10,11]. It is, however, not easy to directly interface mechanical actions by silicon electronics without innovative designs and approaches. Traditionally, signals from strain-sensitive transducers can be probed and acquired by electronic devices. These signals, however, cannot be directly utilized to control silicon electronics. One major focus in the current research of flexible electronics is to minimize and eliminate the effect of strain induced by the substrate on the operations of the electronic components, which can be termed as the passive flexible electronics. On the other hand, the deformation introduced by the substrate can be utilized to induce electrical signals for directly controlling Si-based electronics. The concept of piezotronics and piezo-phototronics is invented for implementing the active flexible electronics [8,9,11], which enables the novel approach for directly generating electronic controlling signals using mechanical actions. The role anticipated to be played by piezotronics is similar to mechanosensation in physiology. The physiological foundation for the senses of touch, hearing, and balance is the conversion of mechanical stimuli into neuronal signals that are the electrical controlling signals. For instance, mechanoreceptors of the skin are responsible for touch, while tiny cells in the inner ear are responsible for hearing and balance. Furthermore, the piezo-phototronic effect can be applied to directly control the charge-carrier separation and recombination processes in a solar cell and in a light-emitting diode (LED), respectively, aiming at improving energy efficiency. This paper is to give a review on the current progress in these fields.

PIEZOTRONIC EFFECT AND PIEZOTRONICS

Piezopotential in piezoelectric semiconductors

In order to realize augmented capabilities, such as interfacing between machine and human/ambient, a direct control over the operation of electronic

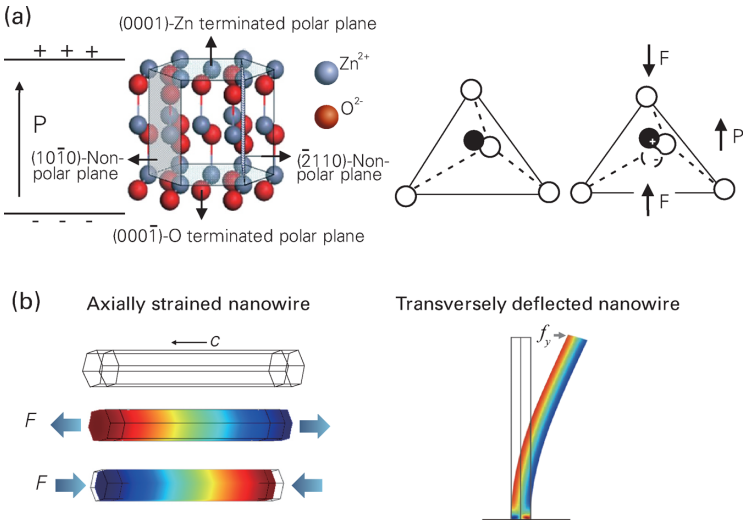

Figure 2. Piezopotential in a wurtzite crystal. (a) Atomic model of the wurtzite-structured ZnO [10] (Copyright 2012 WILEY-VCH, Weinheim). (b) Left: the distribution of piezopotential along a ZnO NW under axial strain calculated by numerical methods [29] (Copyright 2009 American Institute of Physics). Right: the distribution of piezopotential along a transversely deflected ZnO NW calculated by numerical methods [27] (Copyright 2007 American Chemical Society). The color gradient represents the distribution of piezopotential in which red indicates positive piezopotential and blue indicates negative piezopotential. The growth direction of the NW is along the *c*-axis.

devices by mechanical action is highly desired. Piezoelectric materials produce electrical potential upon variations of applied pressure/stress that can be interpreted as the linear electromechanical coupling/interaction between the mechanical and electrical states in materials that lack inversion symmetry [12]. Piezoelectricity has been observed in numerous materials from ceramics, polymers to biological materials. The most well-known piezoelectric material is perovskite-structured $Pb(Zr_xTi_{1-x})O_3$ (PZT) that has been widely used for electromechanical sensing, actuating, and energy harvesting [13–15]. PZT, however, is electrically insulating and is hence less useful for building electronic devices. In addition, the extremely brittle nature of ceramic PZT films and the incorporation of lead impose issues, such as reliability, durability, and safety for long-term sustainable operations, and hinder its applications in areas, such as biomedical devices. On the other hand, wurtzite-structured semiconductor materials, such as ZnO, GaN, InN, and CdS, also possess piezoelectric properties but are not as extensively utilized in piezoelectric sensors and actuators as PZT due to their relatively small piezoelectric coefficients [16].

Wurtzite (ZnO) crystal has a hexagonal structure with a large anisotropic property in the direction of the *c*-axis and perpendicular to the *c*-axis. The Zn^{2+} cations and O^{2-} anions are tetrahedrally coordinated, and the centers of charge of the positive and negatives ions overlap with each other. If a stress is applied at an apex of the tetrahedron, the centers of charge of the cations and anions are relatively displaced, inducing a dipole moment (Fig. 2a). A constructive addition of all the dipole moments within the crystal results in a macroscopic potential drop along the straining direction in the crystal. This is the piezoelectric potential (*piezopotential*) (Fig. 2b) [16]. Piezopotential is a strain-induced inner-crystal field, which is created by non-mobile and non-annihilative ionic charges. Therefore, piezopolarization charges and piezopotential exist as long as the applied strain is maintained. Piezopotential can also drive the flow of electrons in the external load when the materials are subjected to mechanical deformation, which is the fundamental of the nanogenerator [17,18]. The distribution of piezopotential has been investigated based on two typical configurations of a nanowire (NW) devices: the transversely deflected NW and the axially strained NW [Fig. 2b]. Transversely deflected NWs are normally utilized in energy harvesting applications [19], while axially strained NWs are used in piezotronic applications on flexible substrates [20]. The finite conductivity possessed by the material can partially screen the piezo-polarization charges accordingly, but cannot completely diminish them due to the dielectric property of the material and the moderate doping level. Recently, theoretical study has also revealed that a strong piezoelectric field may be induced inside the NW heterostructures due to lattice mismatch, which may introduce significant effects on the charge-carrier transport and confinement [21,22].

Piezopotential distribution in a transversely deflected NW

The configuration of a transversely bent NW is commonly utilized in a nanogenerator and some piezotronic applications [23–26]. The relationship between the piezopotential distribution in a laterally bent NW and the dimensionality of the NW as well as the magnitude of the applied force at the tip has been derived analytically by applying the perturbation expansion of the linear equations [27], which shows that the electric potential (in cylindrical coordinates) is independent of vertical height except for the regions very close to the fixed end of the NW. Moreover, the analytical solution also suggests that the electrostatic potential is directly related to the aspect ratio of the NW instead of its absolute dimensionality. For an NW with a fixed aspect ratio, the induced piezopotential is proportional to the maximum deflection at the NW tip. The schematic

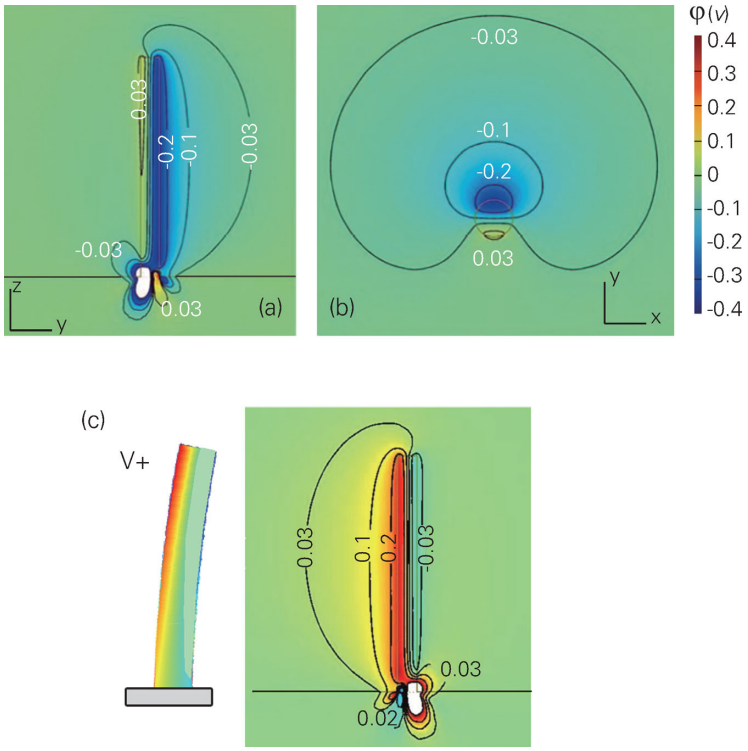

Figure 3. (a,b) Numerical calculation results of the piezopotential distribution in an n-type ZnO NW considering finite doping with a donor concentration of 1×10^{17} cm^{-3} [31] (Copyright 2009 American Chemical Society). (c) Numerical calculation results of the piezopotential distribution when the acceptor concentration in the ZnO NW is 1×10^{17} cm^{-3} [33] (Copyright 2009 American Chemical Society).

illustration of the piezopotential distribution in transversely deflected NWs is shown in Fig. 2b. The validity of the derived analytical equation for the piezopotential distribution in a transversely deflected NW has also been verified by comparing the analytical solutions and finite element method (FEM) calculation for a fully coupled electromechanical system [27], showing that the difference between the results derived from the analytical equation and those from full numerical calculation is only 6%. The response in electrical transport and photoconduction behaviors of the transversely bent ZnO NW due to piezoelectric polarization has also been experimentally studied by *in situ* transmission electron microscopy [28].

Piezopotential distribution in an axially strained NW

Another commonly encountered configuration for the ZnO-NW-based nanoelectronic device incorporates the horizontally placed NW, with its two ends and adjacent regions fully covered by metal electrodes on the substrate (normally flexible material). The dimension of NWs is orders of magnitude smaller than that of the supporting substrates, so that the mechanical behavior of the entire device is dictated by the substrate. In reality, various kinds of forces, including tensile, compression, twisting, and combinations of them, might act on the NW during operation [29]. The distribution of piezopotential throughout the NW under these forces can be obtained by the FEM [29]. For simplicity and concentrating on how the piezopotential would vary under different strains, it is assumed that there is no body force and no free-charge carriers in the NW. It can be seen from Fig. 2b that piezopotential continuously drops from one side of the NW to the other upon straining, indicating that electron energy also continuously increases from one end of the NW to the other. Meanwhile, the Fermi level remains flat all over the NW at equilibrium. Consequently, the electron energy barrier between ZnO and metal electrodes will be raised at one side and lowered at the other side, which should lead to experimentally observable asymmetric *I*–*V* characteristics for the NW device. This is the governing principle of piezotronics and piezo-phototronics [10,11].

Piezopotential distribution in a doped semiconductor NW

It is also important to point out that the above results are all based on an assumption that there are no free-charge carriers in materials [29]. The as-synthesized ZnO nanostructures are, however, intrinsically n-type with a typical donor concentration of 1×10^{17} cm^{-3} [30]. Taking the statistical electron distribution into account, the distribution of piezopotential in a bent ZnO NW with moderate charge-carrier density can be calculated, showing that free electrons tend to accumulate at the positive piezopotential side of the NW at thermal equilibrium [31]. Therefore, the effect of negatively charged carriers partially, if not all, screens the positive piezopotential, while no change to the negative piezopotential can be observed. Fig. 3a and b shows the calculated piezopotential when the donor concentration in the ZnO NW is 1×10^{17} cm^{-3}, which clearly presents the screening effect of finite donor concentration on the distribution of piezopotential [31]. This is also consistent with the experimental observation that only negative pulses can be observed in an atomic force microscopy (AFM)-based nanogenerator experiment using n-type ZnO NWs, and the output negative potential peak appears only when the AFM tip touches the compressed side of the NW [19]. For even smaller systems, strong confinement effect requires quantum-mechanical considerations due to discrete bound states in the materials. In such a case, an elaboration of theory similar to two-dimensional electron gas (2DEG) in GaN/AlGaN

high-electron-mobility transistors (HEMTs) is necessary for investigating the effect of piezopotential [32]. In addition to the n-type doping normally observed for as-synthesized ZnO NWs, it is also possible to receive stable p-type ZnO NWs [33–36]. The stability of p-type doping in ZnO NWs is possible due to the dislocation-free volume and the presence of a high concentration of vacancies near the surface of the NWs [37]. The distribution of piezopotential in a bent p-type ZnO NW has also been theoretically investigated. Fig. 3c shows the calculated piezopotential when the acceptor concentration in the ZnO NW is 1×10^{17} cm^{-3} [33]. With finite p-type doping, the holes tend to accumulate at the negative piezopotential side. The negative side of piezopotential is thus partially screened by holes, while the positive side of it is preserved. Investigating the piezotronic effect in a p-type piezoelectric semiconductor is critical for developing a complete piezotronic theory and designing/fabricating novel piezotronic applications with more complex functionality. Recently, using a low-temperature solution method, ultralong (up to 60 μm in length) Sb-doped p-type ZnO NWs were produced on both rigid and flexible substrates [36], which broadens the scope of piezotronics and extends the framework for its potential applications in electronics, optoelectronics, smart micro/nano-electromechanical system (MEMS/NEMS), and human–machine interfacing.

Piezotronic effect

When a strain is applied along the ZnO NW, which grows in the *c*-axis direction, due to the coupling of piezoelectric and semiconducting properties, piezoelectric polarization charges created at the two ends of the NW induce the piezopotential. This potential is capable of modulating characteristics of the contact formed between the NW and the electrodes by modifying the local Schottky-barrier height (SBH) [16,38,39]. Consequently, the transport of charge carriers in the device can be tuned by the externally applied strain. This is the piezotronic effect [10,16,40]. Electronics fabricated by using the inner-crystal piezopotential as a 'gate' voltage to modulate the charge transport across a metal–semiconductor (M–S) interface or a p–n junction is piezotronics, which is different from the basic design of a complementary metal–oxide–semiconductor (CMOS) field effect transistor (FET) and may enable potential applications in force/pressure-triggered/controlled electronic devices, sensors, biomedical diagnosis/therapy, human–computer interfacing, and prosthetics.

Effect of piezopotential on metal–semiconductor contact

The M–S contact is a fundamental structure of semiconductor electronics and optoelectronics [41]. When a metal and a semiconductor come into contact to form an M–S interface, a significant redistribution of charge takes place due to the overlap of wave functions from both the metal and the semiconductor [42,43]. When the system reaches thermal equilibrium, Fermi levels on either side of the interface must be aligned, and thus a net charge transfer will occur at the interface. If the electron affinity of the semiconductor $e\chi$ (relative to free-electron energy or vacuum level E_0) is appreciably smaller than the work function of the metal $e\phi_m$, then electrons flow into the metal from the semiconductor with the depletion region formed in the semiconductor near the interface. This results in the deformation of energy bands in the semiconductor close to the M–S interface and consequently the formation of an abrupt discontinuity or an energy barrier at the interface that is the Schottky barrier with a barrier height of $e\phi_{Bn}$. Ideally, the intrinsic SBH can be determined by $e\phi_{Bn} = e(\phi_m - \chi)$ (for the n-type semiconductor). The SBH is a measure of the mismatch of energy levels for majority carriers across the M–S interface, which dictates the transport of charge carriers across the M–S interface and is of vital importance for the operation of a related semiconductor device. Current can only pass through the barrier if the externally applied positive bias on the metal is larger than a certain threshold value ϕ_i (for the n-type semiconductor). If the semiconductor material also possesses piezoelectric property, once the strain is induced in the semiconductor, the negative piezoelectric polarization charges and hence the negative piezopotential induced at the semiconductor side can repel the electrons away from the interface, resulting in a further depleted interface and an increased local SBH (Fig. 4a); on the other end, if the polarity of the induced strain is reversed, the positive piezoelectric polarization charges and the positive piezopotential created at the semiconductor side near the interface can attract the electrons toward the interface, resulting in a less depleted interface and hence a decreased local SBH (Fig. 4b) [16,44]. It is well known that the transport of charge carriers across the Schottky barrier is sensitively dictated by the SBH [42]. It can therefore be seen that piezopotential is able to effectively modulate the local contact characteristics depending on the crystallographic orientation of the piezoelectric semiconductor material and the polarity of the applied strain [16]. Consequently, the transport of charge carriers across the M–S contact can be effectively modulated

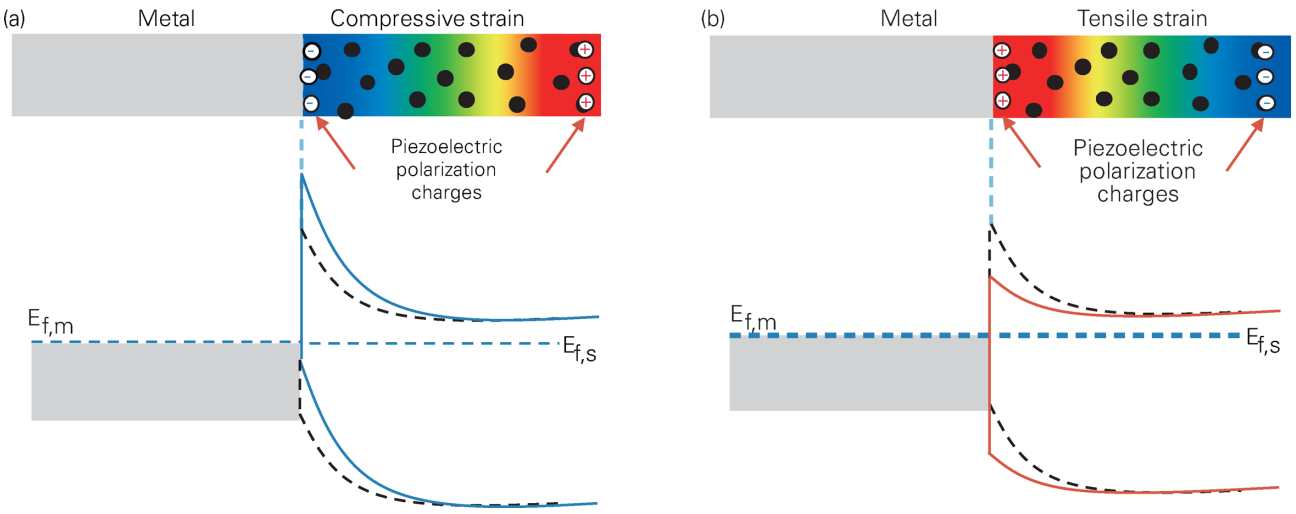

Figure 4. Schematic of energy diagram illustrating the effect of piezopotential on modulating the metal–semiconductor characteristics. (a) With compressive strain applied, the negative piezoelectric polarization ionic charges induced near the interface (symbols with '−') increases the local SBH. (b) With tensile strain applied, the positive piezoelectric polarization ionic charges induced near the interface (symbols with '+') decreases the local SBH. The color gradients indicate the distribution of piezopotential, with red representing positive piezopotential and blue representing negative piezopotential. The band diagrams for the M–S contact with and without the presence of piezotronic effect are shown using the solid and black dashed curves, respectively. The black dots represent the free-charge carriers in the bulk semiconductor. Adapted from [44].

by the piezoelectric polarization charges, or more specifically, the local contact characteristics can be tuned and controlled by varying the magnitude and polarity of externally applied strain. The modulation and gating of charge transport across the interface by the strain-induced piezopotential are the core of piezotronics [16,38].

Effect of piezo-charges on the p–n junction

A p–n junction consists of two semiconductor regions with an opposite doping type is another fundamental building block in modern electronics and optoelectronics [45]. When the p- and n-type semiconductors form a junction, the holes on the p-type side and the electrons on the n-type side adjacent to the metallurgical junction tend to diffuse across the junction into the n-type/p-type region where few holes/electrons are present and redistribute to balance the local potential and reach thermal equilibrium. This diffusion process leaves ionized donors or acceptors behind, creating the charge depletion zone close to the junction that is depleted of mobile carriers. The ionized donors and acceptors induce an electric field that in turn results in the drift of charged carriers, moving in the opposite direction to that of the diffusion process. The diffusion of carriers continues until the drift current balances the diffusion current, thereby reaching the thermal equilibrium of the system, as indicated by the aligned Fermi energy across the system. As per the discussions on piezopotential in the previous sections, the presence of such a carrier depletion zone can significantly enhance the piezotronic effect due to the fact that the piezoelectric polarization charges will be preserved, since the amount of regional residual free carriers is negligible in the charge depletion zone [16]. For simplicity, the p–n homojunction is considered in which the bandgaps for both p- and n-type materials are the same. Meanwhile, only the n-type material is piezoelectric. Once the strain is induced in the n-type semiconductor, the positive piezoelectric polarization charges and hence the positive piezopotential induced in the n-type region close to the junction interface attract the electrons toward the interface, resulting in the trapping or accumulation of electrons adjacent to the interface and thus a dip in the local band profile (Fig. 5a) [16], which might be beneficial for promoting the electron–hole recombination and improving the efficiency of LED applications [46]. Furthermore, the inclined band profile can also modulate the mobility of charged carriers moving toward the junction. On the other hand, if the polarity of the induced strain is reversed, the negative piezopotential created in the n-type region close to the junction interface can repel the electrons away from the interface, resulting in the depletion of electrons adjacent to the interface and thus a shoulder in the local band profile (Fig. 5b) [16]. This may result in the suppression of the electron–hole recombination rate in the device, which could be detrimental for related optoelectronic applications [46]. More complicated situations involving p–n heterojunctions (in which the bandgaps for both p- and n-type materials are different) can be discussed accordingly. Similar discussions can also be easily

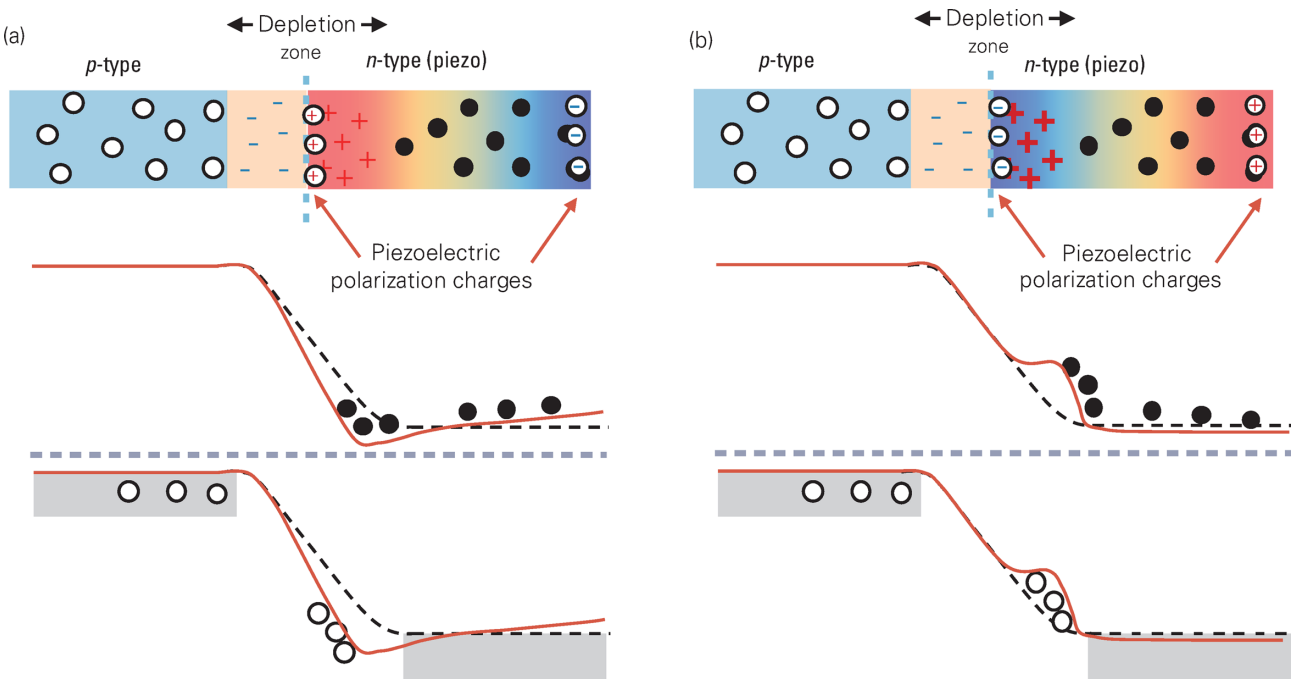

Figure 5. Schematic of energy diagram illustrating the effect of piezopotential on modulating characteristics of the p–n homojunction. With strain applied, the piezoelectric polarization ionic charges are induced near the junction interface. The color gradients in (a) and (b) indicate the distribution of piezopotential, with red representing positive piezopotential and blue representing negative piezopotential. The band diagrams for the p–n junction with and without the presence of piezotronic effect are shown using the red solid and black dashed curves, respectively. $E_{f,n}$ and $E_{f,p}$ are the Fermi levels in n- and p-type materials, respectively. E_0 and E_i are the vacuum level and intrinsic Fermi level, respectively. The black dots and empty circles represent the free-charge carriers in the semiconductor. Symbols '+' and '−' represent the ionized donors and acceptors in respective regions. Adapted from [44].

extended to cases including p-type piezoelectric semiconductor materials.

Basic theory of piezotronics

Theoretical efforts have also been made to derive analytical expressions for revealing the working principle of the piezotronic device [47]. The mechanical and electromechanical properties of piezoelectric NWs have been investigated in detail as well [48]. In the following sections, corresponding discussions will be provided on the piezotronic effects in M–S contacts and p–n junctions.

Piezotron effect in metal–semiconductor contact

By ignoring surface states and other anomalies, space charge distribution, electric field, and energy-band diagram in the M–S contact with the presence of piezoelectric polarization charges at the zero applied voltage (thermal equilibrium) are shown in Fig. 6a, in which W_n is the width of the region where ionized donors are distributed in the n-type semiconductor (ZnO here). When the strain is introduced in the semiconductor, the induced polarization charges at the interface not only change the height of the Schottky barrier, but also the width of the depletion region. The carrier transport in the M–S contact is dominated by the majority carriers according to the diffusion theory for the Schottky barrier, and the current under the forward bias can be expressed as [49]

$$J_n \approx J_D \cdot [\exp(qV/kT) - 1],$$

where

$$J_D \approx q^2 D_n N_C \cdot (kT)^{-1} \cdot \sqrt{[2q N_D(\psi_{bi} - V) \cdot \varepsilon_s^{-1}]} \cdot \exp[-q\phi_{Bn} \cdot (kT)^{-1}]$$

is the saturation current density. Here ε_s is the permittivity of the semiconductor material, D_n is the diffusion coefficient for electrons, N_C is the effective density of states in the conduction band, and N_D is the donor concentration in the semiconductor. The saturation current density with the absence of the piezoelectric polarization charge is

$$J_{D0} \approx q^2 D_n N_C \cdot (kT)^{-1} \cdot \sqrt{[2q N_D(\psi_{bi0} - V) \cdot \varepsilon_s^{-1}]} \cdot \exp[-q\phi_{Bn0} \cdot (kT)^{-1}],$$

where ψ_{bi0} and ϕ_{Bn0} are the built-in potential and SBH, respectively, with the absence of piezoelectric polarization charges. The effect of the piezoelectric charge can be considered as perturbation to the conduction-band edge [47]. The change in the effective SBH induced by piezoelectric polarization charges is then derived as $\phi_{Bn} = \phi_{Bn0} - q^2\rho_{piezo}W_{piezo}^2(2\varepsilon_s)^{-1}$, where piezoelectric polarization charges are distributed in the region with a width of W_{piezo} near the barrier interface. In conventional piezoelectric theory, since the region within which the piezoelectric polarization charges are distributed is much smaller than the volume of the bulk crystal, it is reasonable to assume that piezoelectric polarization charges are distributed at the surface region with the zero thickness of the bulk piezoelectric material. Such an assumption, however, does not hold true for NW devices. The current density across the Schottky barrier formed between the metal and strained n-type piezoelectric semiconductor can hence be rewritten as

$$J_n \approx J_{D0}\cdot\exp[q^2\rho_{piezo}W_{piezo}^2(2kT\varepsilon_s)^{-1}]\cdot\exp[qV\cdot(kT)^{-1}-1].$$

A more specific expression can be obtained to reflect the effect of piezopotential on metal–wurtzite semiconductor (such as ZnO NW) contact. If the induced strain is s_{33} along the *c*-axis of the ZnO NW, the piezoelectric polarization can then be obtained from $P_z = e_{33}s_{33} = q\rho_{piezo}W_{piezo}$, where ρ_{piezo} represents the density of created piezoelectric polarization charges (in units of electron charge). The current density across the Schottky barrier is now expressed as

$$J \approx J_{D0}\cdot\exp[qe_{33}s_{33}W_{piezo}\cdot(2kT\varepsilon_s)^{-1}]\cdot\exp[qV\cdot(kT)^{-1}-1].$$

It can be clearly seen that the current transported across the M–S interface is directly related to not only the magnitude, but also to the polarity of the induced strain. When positive piezoelectric polarization charges (positive ρ_{piezo}) due to tensile strain (positive s_{33}) are introduced locally to the Schottky barrier at work, the current transported across the barrier increases. A similar conclusion can also be achieved when the polarity of the induced strain is switched to compressive type. This is the fundamental mechanism of piezotronic devices, such as strain-gated transistors (SGTs) [38].

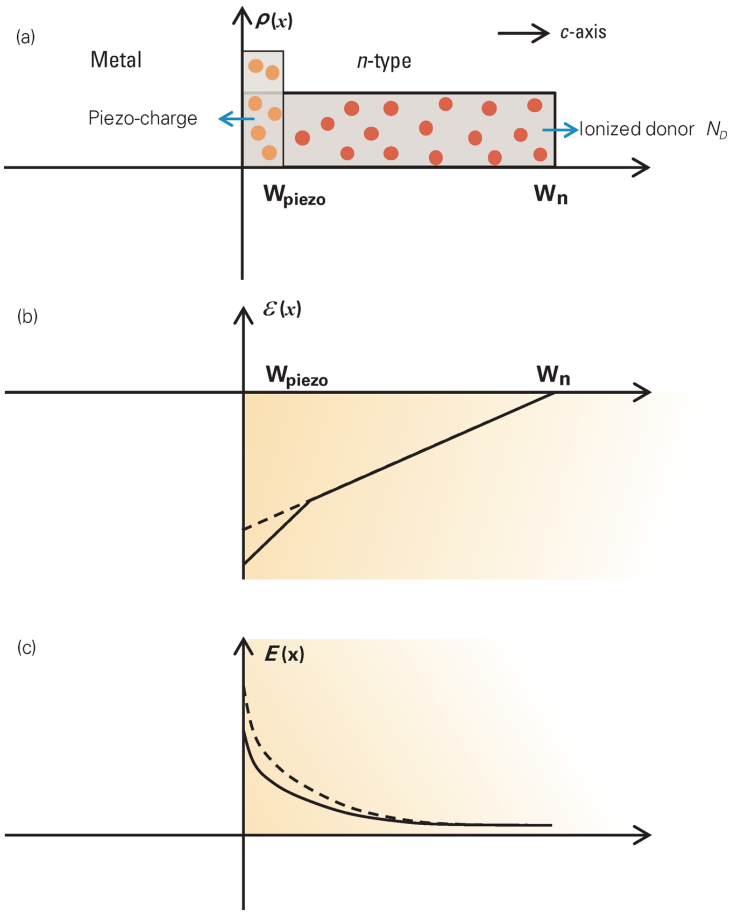

Figure 6. (a) Space charge distribution; (b) electric field, and (c) energy-band diagram for ideal metal–semiconductor Schottky contacts with the presence of piezoelectric polarization charges at the applied voltage $V = 0$ (thermal equilibrium). The dashed lines indicate the electric field and energy band with the absence of piezoelectric charges. Adapted from [47].

Piezotronic effect in p–n junctions

Shockley theory provides the fundamental of *I*–*V* characteristics of the piezoelectric p–n junctions [50]. For simplicity, we assume that the p-type region is non-piezoelectric and n-type region is piezoelectric. Considering the fact that the ZnO NW grows along the direction of the *c*-axis, the positive charges are created at the n-type side of the p–n junction by applying a compressive stress along the *c*-axis. An abrupt junction model is used here, in which the impurity concentration in a p–n junction changes abruptly from the acceptor N_A to the donor N_D. The built-in potential is given by

$$\psi_{bi} = q\cdot(2\varepsilon_s)^{-1}\cdot(N_AW_{Dp}^2 + \rho_{piezo}W_{piezo}^2 + N_DW_{Dn}^2),$$

where $N_D(x)$ is the donor concentration, $N_A(x)$ is the acceptor concentration, and W_{Dp} and W_{Dn} are the depletion layer widths in the p-side and the n-side, respectively [47].

This suggests that the change in the built-in potential can be modulated by the strain-induced piezoelectric charges. For a simple case in which the n-type side has an abrupt junction with the donor concentration N_D, and locally $p_{n0} \gg n_{p0}$, where p_{n0} is the thermal equilibrium hole concentration in an n-type semiconductor and n_{p0} is the thermal equilibrium electron concentration in a p-type semiconductor, the total current density of the p–n-junction-based piezotronic transistor is given by

$$J = J_{C0} \cdot \exp[q^2 \rho_{piezo} W_{piezo}^2 (2kT\varepsilon_s)^{-1}] \cdot \exp[qV \cdot (kT)^{-1} - 1],$$

where J_{C0} is the saturation current density with the absence of piezopotential [47].

This shows that the current transported across the p–n junction is an exponential function of the density of local piezo-charges, the sign of which depends on the type of strain. Therefore, the carrier transport can be effectively modulated by not only the magnitude of the strain, but also by the sign of the strain (tensile or compressive).

PIEZOTRONIC EFFECT IN ELECTRONICS AND SENSING APPLICATIONS

Mechanical straining can create a piezopotential inside ZnO due to the polarization of the non-mobile ions. Piezopotential can act as a controlling signal for gating the charge-carrier transport, which is the fundamental principle for strain-gated piezotronic devices, based on which the ZnO-NW electromechanical switch and diode are fabricated [20,51,52]. The mechanical–electrical coupled and controlled actions can then be performed in one structure unit made of a single material.

Strain-gated piezotronic transistors and logic operations [38]

By using the piezopotential as the 'gating voltage' for modulating the charge transport, the fundamental principle and implementation of piezotronic transistors using horizontally and vertically aligned NWs have been presented [38,53,54]. The piezotronic transistor is a two-terminal device without the presence of an electrical gate electrode. The replacement of an external gating voltage by the inner-crystal potential makes it possible to fabricate the arrays of devices using vertical NWs that can be individually addressed or controlled [54]. This is advantageous for fabricating a high-density device matrix in electromechanical transduction, such as sensors array and touch-pad applications. Piezopotential is also capable of modulating the channel conductivity of other heterogeneous electronics [55].

An SGT can be made of a single ZnO NW with its two ends being fixed by metal contacts, which are the source and drain electrodes, on a polymer substrate (Fig. 7a). Once the substrate is bent, a tensile/compressive strain is created in the NW, since the mechanical behavior of the entire structure is determined by the substrate due to the significant difference in dimensions between the NW and the substrate. For an SGT, the external-mechanical-perturbation-induced strain (ε_g) acts as a gate input for controlling the 'on'/'off' state of the NW SGT. The positive/negative strain is created when the NW is stretched/compressed. The I_{DS}–ε_g curves at a fixed V_{DS} show that I_{DS} increases as the gate strain ε_g increases and the threshold gate strain ε_T is ~0.08% (Fig. 7b). The working principle of an SGT is illustrated by a band structure of the device. An externally applied mechanical strain (ε_g) results in both the band structure change and piezopotential field inside a ZnO NW. The change in the band structure leads to the piezoresistive effect that is a

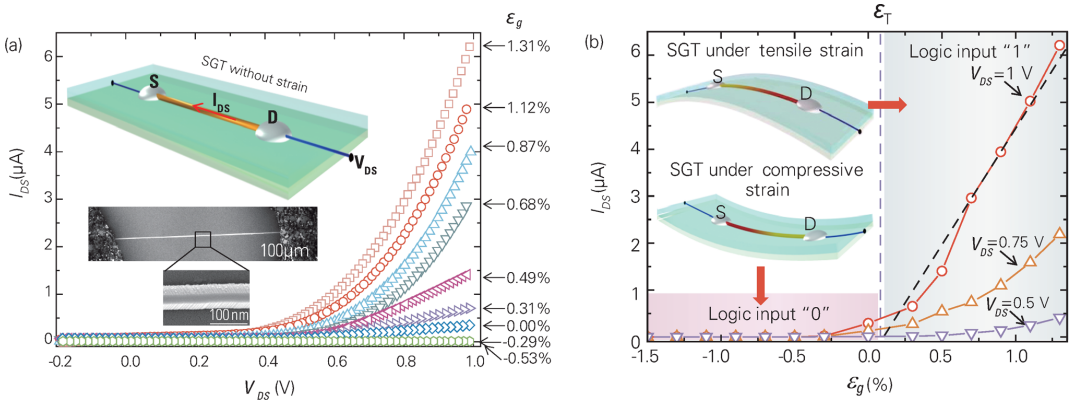

Figure 7. Single ZnO NW SGT. (a) I_{DS}–V_{DS} output characteristic for a ZnO SGT device. (b) I_{DS}–ε_g transfer characteristic for the same ZnO SGT device under three different V_{DS} bias values: 1, 0.75, and 0.5 V [38] (Copyright 2010 WILEY-VCH, Weinheim).

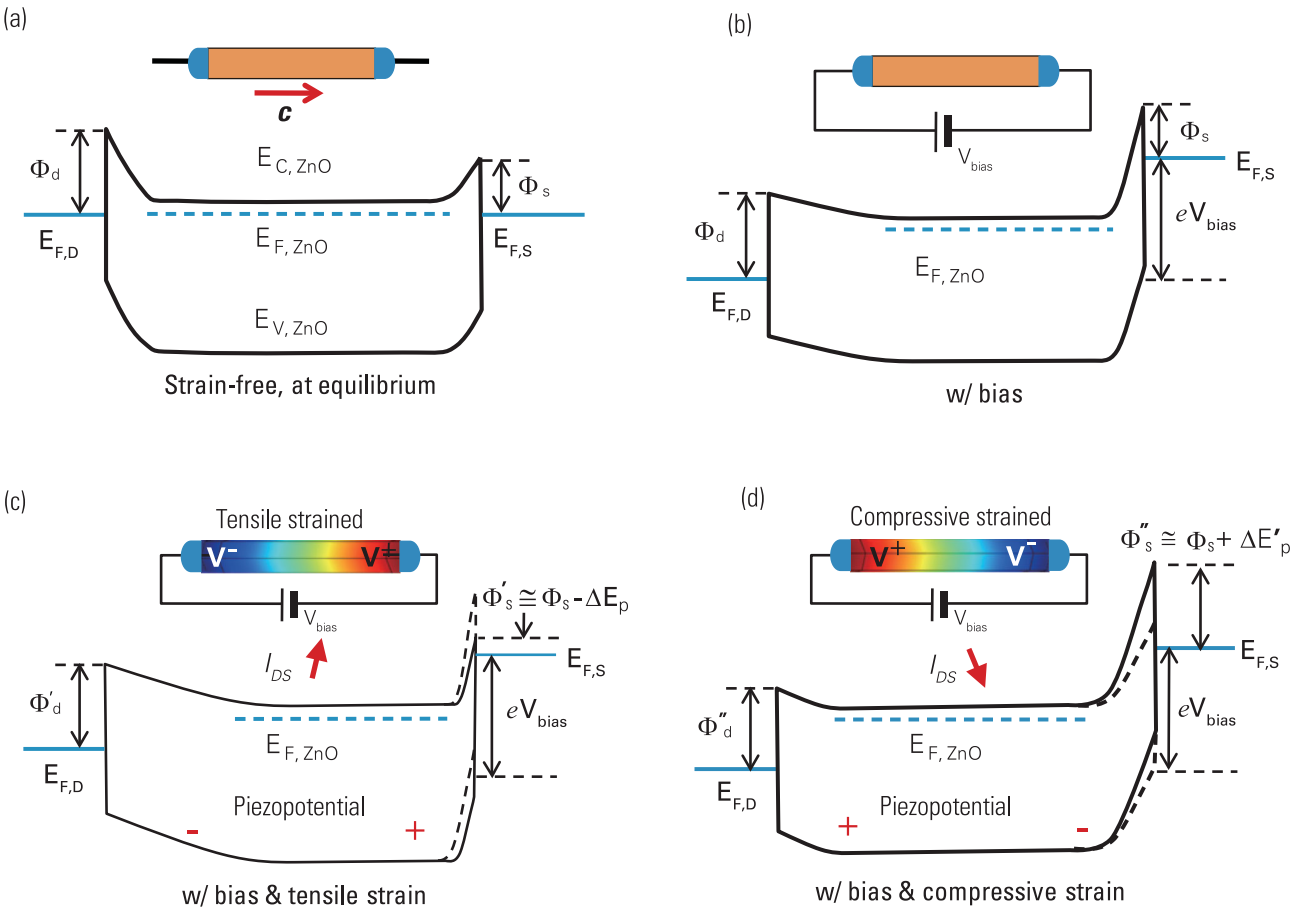

Figure 8. The band structures of the ZnO NW SGT under different conditions for illustrating the mechanism of the SGT. (a) The band structure of a strain-free ZnO NW SGT at equilibrium with different barrier heights of Φ_S and Φ_D at the source and drain electrodes, respectively. (b) The quasi-Fermi levels at the source ($E_{F,S}$) and drain ($E_{F,D}$) of the ZnO SGT are split by the applied bias voltage V_{bias}. (c) With tensile strain applied, the SBH at the source side is reduced from Φ_S to $\Phi'_S \cong \Phi_S - \Delta E_P$. (d) With compressive strain applied, the SBH at the source side is raised from Φ_S to $\Phi''_S \cong \Phi_S + \Delta E_P$ [38] (Copyright 2010 WILEY-VCH, Weinheim).

non-polar and symmetric effect at both the source and drain contacts. Since ZnO is a polar structure along the *c*-axis, straining in the axial direction (*c*-axis) creates a polarization of cations and anions in the NW growth direction, resulting in a piezopotential drop from V^+ to V^- inside the NW (Fig. 8), which produces an asymmetric effect on the changes in the SBHs at the drain and source electrodes. Under tensile strain, the SBH at the source side decreases from Φ_S to $\Phi'_S \cong \Phi_S - \Delta E_P$ (Fig. 8c), where ΔE_P denotes the change from the locally created piezopotential and is a function of the applied strain, resulting in the increased I_{DS}. For the compressively strained SGT, the sign of the piezopotential is reversed, and thus the SBH at the source side is raised from Φ_S to $\Phi''_S \cong \Phi_S + \Delta E'_P$ (Fig. 8d), where $\Delta E'_P$ denotes the piezopotential effect on the SBH at the source side, resulting in a large decrease in I_{DS}. Therefore, as the strain ε_g is swept from compressive to tensile regions, the I_{DS} current can be effectively turned from 'on' to 'off', while V_{DS} remains constant. This is the fundamental operating principle of the SGT. A better illustration of the basic concept of piezotronics can be obtained by comparing the SGT with the conventional metal–oxide–semiconductor-FET (MOSFET), as shown in Fig. 9 [56]. A comparison between the piezotronic effect and commonly recognized piezoresistive effect is listed in Table 1 [56]. The piezotronic strain-gated complementary logic gates can then be built using back-to-back packaged n-type ZnO NW SGTs on the top and bottom surfaces of the same flexible substrate. Universal logic operations, such as inverters, NAND, NOR, XOR gates, have been demonstrated for performing piezotronic logic calculations, which have the potential to be integrated with the MEMS technology for achieving advanced and complex functional actions [38]. Recently, basic piezotronic computation, such as 1-bit binary addition over the input mechanical strains with corresponding computation results

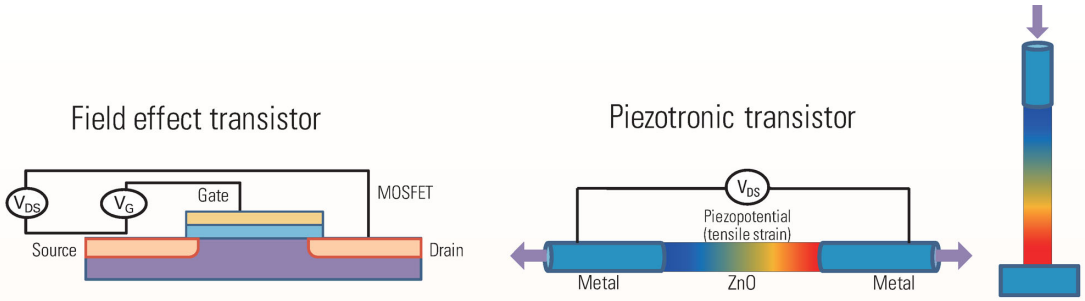

•**Control:**	External applied voltage Channel width control	Self-generated inner-crystal potential Interface/junction control
•**Gate:**	Voltage	Strain/deformation
•**Structure:**	3-terminal (S, D, G)	2-terminal
•**Materials:**	Si (Ge, GaAs …)	Wurtzite (ZnO, GaN …)
•**Speed:**	Fast (GHz)	Slower (KHz, MHz)
•**Applications:**	Computation, logic, Sensors, photonics	Human/environmental interfacing, MEMS, photonics (piezo-phototronic,effect)

Figure 9. Comparison between a traditional FET and an SGT [56] (Copyright 2013 American Chemical Society).

Table 1. Comparison between piezoresistive effect and piezotronic effect [56]. (Copyright 2013 American Chemical Society).

Piezoresistive effect	Piezotronic effect
Linear *I–V* curve	Nonlinear 'rectifying' *I–V* curve
Symmetric effect on end-contacts	Asymmetric effect on end-contacts
No polarity	Strong polarity
'Volume' effect	'Interface' effect
No switch function	Switch function

in an electrical domain by half-adder, has been implemented using GaN-nanobelt-based strain-gated piezotronic logic devices [56].

Piezotronic NW electromechanical memories [39]

Based on the piezotronic effect discussed above, the piezoelectrically modulated resistive switching device based on the ZnO NW has been demonstrated, through which the write/read access of the memory cell is programmed via electromechanical modulation [35]. Adjusted by the strain-induced polarization charges created at the semiconductor/metal interface under externally applied deformation, the resistive switching characteristics of a cell can be modulated in a controlled manner, and the logic levels of the strain stored in the cell can be recorded and read out, which has the potential for integrating with NEMS technology to achieve MNSs capable for intelligent and self-sufficient multi-dimensional operations [39,57–59].

The external-mechanical-perturbation-induced strain (ε_g) acts as a programming input for modulating the hysteretic *I–V* characteristics of a piezoelectrically modulated resistive memory (PRM) cell. A positive/negative strain is created when the ZnO NW is stretched/compressed. An interesting phenomenon was observed when a PRM cell experienced straining (Fig. 10a). When the PRM cell was tensile stretched ($\varepsilon = 1.17\%$), the hysteretic switching curve shifted toward the lower voltage side by 1.49 V (the red line in Fig. 10a); when the cell was compressively deformed ($\varepsilon = -0.76\%$), the hysteretic switching curve shifted toward the higher voltage side by 1.18 V (the blue line in Fig. 10a). $V_{th,S+}$, $V_{th,S0}$, $V_{th,S-}$ and $V_{th,D+}$, $V_{th,D0}$, $V_{th,D-}$ are the threshold switching voltages for the PRM cell with tensile, zero, and compressive strains, respectively. The ratios of conductance between a low-resistance state (LRS) and a high-resistance state (HRS) for the PRM cell remain steady at high values ($\sim 10^5$) under different strains, demonstrating the stable performance of the cell and its potential feasibility for applications in flexible memory and logic operations [38]. The intrinsic rectifying behavior of the PRM cell may

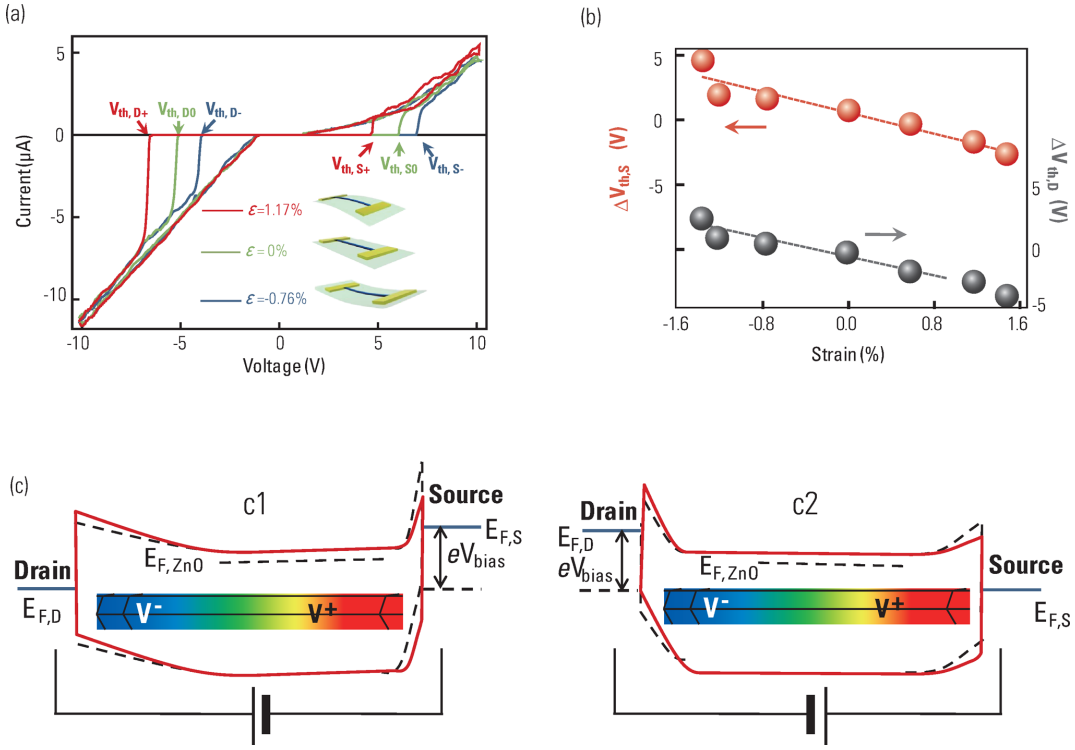

Figure 10. Stain-modulated hysteretic switching of PRM cell. (a) *I–V* characteristics of ZnO PRM cells under tensile, zero, and compressive strains. (b) Dependence of threshold voltages on applied strains. (c) Schematic of the band diagram of the PRM cell under tensile strain. C1, Schottky barrier at the drain side is forward-biased. C2, Schottky barrier at the drain side is reversely biased. The red solid lines represent the band diagrams after tensile strain is applied. The black dashed lines represent the band diagrams under the strain-free condition [39] (Copyright 2011 American Chemical Society).

solve the sneak path problem as well as reduce the static power consumption [60], which allows for the construction of large passive resistive-switching device arrays. The changes in threshold switching voltages of the PRM cell with different strains have been plotted in Fig. 10b. It can be seen that the change in both the $V_{th,S}$ and $V_{th,D}$ almost linearly depends on strain applied to the PRM cell, while the width of the HRS window ($V_{th,Si} - V_{th,Di}$, where $i = +, 0, -$) remains almost constant for different strain values. The modulation effect of strain on the hysteric switching behavior of the PRM cell can then be explained using the band diagram of the working device (Fig. 10c). If the PRM cell is under tensile strain, with the Schottky barrier at the drain side being forward-biased ($V > 0$ in Fig. 10a), the positive piezoelectric potential resulting from the positive strain-induced polarization charges reduces the SBH at the reverse-biased source barrier, while the negative piezoelectric potential increases the SBH at the forward-biased drain barrier (the red line in Fig. 10c1). Since the *I–V* characteristic is dictated by the reverse-biased source barrier, the existence of the strain-induced piezoelectric potential results in the shift of the switching threshold voltage from $V_{th,S0}$ to $V_{th,S+}$, indicating that only a smaller bias is required to switch the PRM cell from the HRS to LRS. Alternatively, if the Schottky barrier at the drain side is reverse-biased ($V < 0$ in Fig. 10a), the SBH is still reduced at the source barrier, while it is increased at the drain barrier (Fig. 10c2), since the polarity of the strain did not change, and hence the piezoelectric potential remained negative and positive at the source barrier and drain barrier, respectively. The *I–V* characteristic is now dictated by the reverse-biased drain side in this case, and a shift of the switching threshold voltage from $V_{th,D0}$ to $V_{th,D+}$ was observed, indicating that a larger bias has to be applied in order to switch the PRM cell from the HRS to LRS. By the same token, in the case of applying compressive strain to the PRM cell, the shift of the switching threshold voltage from $V_{th,S0}$ to $V_{th,S-}$ and $V_{th,D0}$ to $V_{th,D-}$ can be explained. The PRM can function as an electromechanical memory, in which the write/read access can be programmed via mechanical actuation. A pulse train consisting of several write/read/erase pulses is applied to the

PRM cell to record and read out the polarity/logic levels of the 'stored' strain in the cell by monitoring the characteristic patterns in the output current. A quantitative analysis of the magnitudes of the output currents can give the absolute values of the strains stored in the PRM cells [39].

Taxel-addressable matrix of vertical-NW piezotronic transistors for active/adaptive sensing [54]

Designing, fabricating, and integrating arrays of nanodevices into a functional system are the key for transferring nano-scale science into applicable nanotechnology. The large-array three-dimensional (3D) circuitry integration of piezotronic transistors based on vertical ZnO NWs as an active taxel-addressable pressure/force–sensor matrix for tactile imaging has been recently reported [54]. Using the piezoelectric polarization charges created at the M–S interface under the strain-to-gate/modulate transport process of local charge carriers, the piezotronic effect has been applied to design independently addressable two-terminal transistor arrays that convert mechanical stimuli applied on the devices into local electronic controlling signals. The elimination of the wrap gate offers a new approach for 3D structuring. The basic structure of a 3D strain-gated vertical piezotronic transistor (SGVPT) is depicted in Fig. 11a (right), consisting of one or multiple vertically grown ZnO NWs in contact with the bottom and top electrodes. The ZnO NW experiences the axial strain when subjected to external mechanical deformation, with piezopotential induced inside the NW due to the polarization of non-mobile ions distributed at the two ends [10,11]. The local contact profile and carrier transport characteristics across the Schottky barrier, formed between the ZnO NW and metal electrodes, are effectively controlled by the polarization-charge-induced potential. Electrical characteristics of the two-terminal SGVPT are therefore modulated by the external-mechanical-action-induced strain that essentially functions as a gate signal for controlling the SGVPT. By combining the patterned in-place growth of vertically aligned ZnO NWs with state-of-the-art microfabrication techniques, the large-scale integration of the SGVPT array can be obtained. Fig. 11b illustrates the schematic of the SGVPT array with a taxel density of 92 × 92 in 1 cm^2 (234 taxels per inch). The equivalent circuit diagram of the SGVPT array is displayed in Fig. 11c to demonstrate the strain-gating operation scheme of the SGVPT device circuitry.

The dominant mechanism for the transport property of the SGVPT is the piezotronic effect rather than the piezoresistive effect, as experimentally confirmed and elaborated in detail in [54]. The modulation effect of the applied pressure is shown from the plot of current variations against pressure changes (Fig. 11e). The observed sensing a range of a few kPa to ∼30 kPa for the SGVPT array is well matched to the 10–40 kPa range that a human finger applies to sense texture and shape. The conductance of the SGVPT device is dictated by the reversed-biased Schottky contact that is formed between ZnO NWs and top electrodes in this case. Upon applying the normal stress, the accumulation of piezoelectric charges at both Schottky contacts induces the distribution of the piezopotential. Due to the orientation of the polar *c*-axis in the as-synthesized ZnO NWs (indicated by the red arrow in Fig. 11a), negative piezopotential is induced at the reverse-biased top Schottky contact, which raises the barrier height at that contact and hence decreases the transport conductance of the SGVPT taxel. The operation of the SGVPT device is therefore based on barrier-interface-modulation that enables enhanced sensitivity and efficiency compared to the channel-modulation operation in conventional FETs.

The successful fabrication of the 92 × 92-taxel SGVPT array enables a 15-to-25-fold increase in the number of taxels and 300-to-1000-fold increase in taxel area density compared to recent reports [61–63]. The device matrix has been demonstrated for achieving multi-dimensional active sensing that demonstrates the potential of utilizing the SGVPT array for future applications, such as multi-dimensional signature recognition by not only recording the calligraphy or signature patterns, when people write, but also registering the corresponding pressure/force applied at each location/taxel and writing speed by the person. This augmented capability can essentially provide a means for realizing personal signature recognition with a unique identity and enhanced security. The SGVPT array has also shown the capability of shape-adaptive high-resolution tactile imaging. The real-time detection of shape changes caused by stretching or twisting is a desirable feature for sensors embedded in an artificial tissue or prosthetic device. Moreover, the SGVPT devices can also function as self-powered active tactile sensors by converting mechanical stimulations into electrical signals utilizing the piezopotential without the applied bias, which emulates the physiological operations of mechanoreceptors in biological entities, such as human hair follicles and hair cells in the cochlea. The 3D piezotronic transistor array may have applications in human–electronics interfacing, smart skin, and MEMS/NEMS.

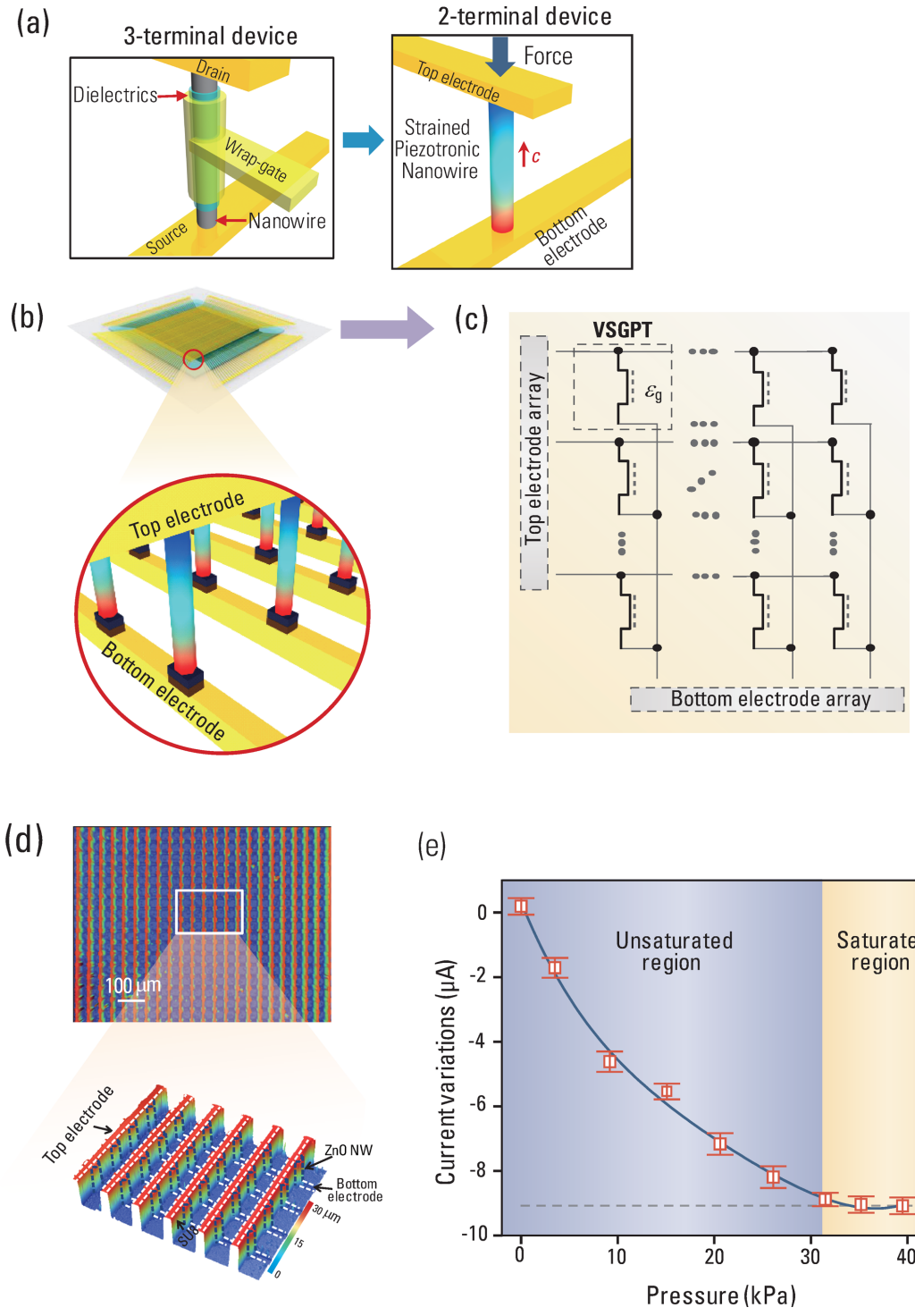

Figure 11. (a) Comparison between a three-terminal voltage-gated NW FET (left) and a two-terminal SGVPT (right). ZnO NWs in the SGVPT grow along the *c*-axis, as indicated by the red arrow. (b) Schematic illustration of a 3D SGVPT array with the taxel density of 92 × 92 and scheme for spatial profile imaging of local stress (indicated by the downward blue arrowhead) by the array (zoom-in schematic). (c) Equivalent circuit diagram of the 3D SGVPT array. The region highlighted by the black dashed lines is the unit SGVPT device, in which ε_g represents the mechanical strain gate signal, and the vertical dotted line between the two terminals of SGVPT presents the modulation effect of ε_g on the conducting characteristics of the device. (d) Topological profile image of the SGVPT array (top view). The inset shows the 3D perspective view of the topological profile image reveals the vertical hierarchy of the SGVPT assembly in which the color gradient represents different heights. (e) Current responses for taxel 46 under different pressures, presenting the gate modulation effect of applied pressure on the electrical characteristics of the SGVPT [54] (Copyright 2013 the American Association for the Advancement of Science).

Piezotronic effect in flexible thin-film-based devices

Currently, almost all of the demonstrated piezotronic devices are based on one-dimensional (1D) wurtzite nanostructures, mostly ZnO NWs. Although 1D nanostructures are promising building blocks for future electronics, technical difficulties in implementing 1D-nanostructure-based devices hinder their immediate applications. Despite the fact that numerous techniques have been reported for the bottom-up synthesis of 1D semiconductor nanostructures [64–68], the lack of uniformity in as-synthesized materials, in terms of dimensions, morphologies, and doping levels, leads to performance inconsistency from device to device. Moreover, the techniques currently available for positioning, aligning, and integrating as-synthesized 1D nanostructures are either cumbersome or incompatible with state-of-the-art microfabrication processes. Specifically for piezotronic applications, in addition to feasibly integrating 1D nanostructures with microfabrication of device architectures and peripheral circuits, determination and engineering control of the polar *c*-axis orientation in as-synthesized nanomaterials, which still remains elusive, is of pivotal importance for further construction of integrated devices/systems. On the other hand, the piezotronic effect is prospected to be a pervasive effect [10] and exists in various semiconductor nanomaterials, such as GaN, $ZnSnO_3$, and CdS [53,69–72]. Moreover, the success of semiconductor technology is enabled by thin-film processing that provides engineering control over material properties as well as scalable integrated fabrication processes. Investigating and utilizing piezotronic effect in thin-film-based material systems could hence potentially circumvent the limitations posed by 1D nanostructures and fully appreciate the state-of-the-art microfabrication technologies.

The first study of the piezotronic effect in radio-frequency-sputtered (RF-sputtered) ZnO thin films was recently carried out [73]. A ZnO thin film with controllable property was grown via RF sputtering on flexible PET substrates. The characterization result indicates that ⟨0 0 0 1⟩, corresponding to the *c*-axis of wurtzite ZnO, is the preferred growth direction and suggests that the as-grown film consists of multiple mesoscopic columnar grains [73]. The alignment of the *c*-axes within these columnar grains gives rise to macroscopically observed piezoelectricity of the ZnO polycrystalline thin film. Piezoelectric tests were performed to determine the polarity of the film, by investigating the strain-induced electrical outputs of as-assembled device, which has a metal–ZnO thin-film-metal structure. It is found that properties of the substrates are crucial in dictating the piezoelectric polarity of the RF-sputtered ZnO thin film. However, the polarity control of the as-sputtered piezoelectric film is complex and non-trivial in the sense that it is not only influenced by substrate properties, but also by sputtering conditions and many other factors, which needs more in-depth investigations. When compressive strain was applied, the current flowing through the device increased, whereas when a tensile strain was applied, the current flowing through the device decreased. To explicitly demonstrate the 'gating' effect of external strain on modulating the charge-carrier transport in the ZnO thin-film piezotronic device, current values (I) in the device under various strains were monitored at a fixed bias. I_0 was the current flowing through the device when no strain was applied. As can be seen from the I/I_0–strain curve in Fig. 12b, the currents in the device corresponding to each strain applied were similar when either the source or the drain electrode was reversely biased. The conductivity of the entire thin film device is dictated by the reverse-biased contact, and the effective conductivity of the device is sensitive to the change in the SBH at that specific contact. Different from previous piezotronic devices based on 1D nanomaterials in which M–S contacts are formed at the two opposite polar surfaces, both source and drain electrodes in the ZnO thin-film piezotronic devices are in contact with the same surface of the as-deposited ZnO film, and hence piezoelectric polarization charges with the same polarity will be induced at both Schottky contacts when external strain is applied. This leads to the observed I–V curves (Fig. 12a), in which the same tuning trend of the applied strain can be observed when either the source or the drain side is reversely biased. As pointed out earlier, this helps circumvent the difficult and elusive predetermination of the *c*-axis' orientation for 1D nanostructures and brings significant simplification and convenience for further construction of integrated devices/systems. It is also demonstrated that the ultraviolet (UV) sensing capability of the as-fabricated thin-film-based piezotronic device can be tuned by piezopotential, showing significantly enhanced sensitivity and improved reset time under tensile strain [73]. Considering the technological compatibility, piezoelectric semiconductor thin films could be the excellent alternative to 1D counterpart for realizing piezotronic applications and broadening the scope of piezotronics to extend its potential applications in sensors [51,69–71,74,75], electronics

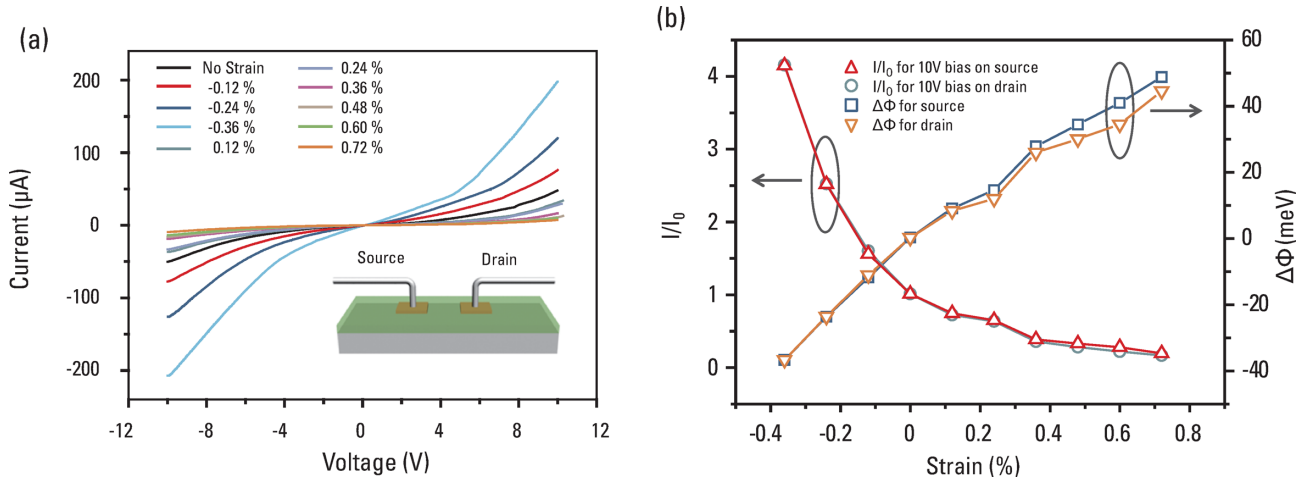

Figure 12. (a) *I–V* curves under different strains were obtained from a device with Schottky-contact electrodes, demonstrating the modulation of charge-carrier transport via piezotronic effect. (b) Calculated changes in current and SBHs explicitly demonstrate the 'gating' effect of external strain on charge-carrier transport in the ZnO thin-film piezotronic device [73] (Copyright 2013 WILEY-VCH, Weinheim).

[38,39,76, 77], optoelectronics [46,72,78–83] and human–machine interfacing [54].

Piezotronic effect in solution-grown p-type ZnO NWs and films

The aforementioned piezotronic devices were all fabricated using intrinsically n-type ZnO, and few studies of piezotronics based on p-type materials, especially p-type ZnO, have been done. In order to develop a full understanding of the theory of piezotronics and enable novel applications in electronics and optoelectronics, it is essential to investigate the feasibility of p-type piezoelectric semiconductors for piezotronic applications. The successful growth of ultra-long Sb-doped p-type ZnO NWs up to 60 μm in length was recently demonstrated using a low-temperature solution growth method [36]. Electrical transport measurement confirmed clear p-type characteristics for both 0.2% and 1% Sb-doped ZnO NWs. The electrical transport characteristic of a 0.2% Sb-doped sample was re-measured after two months, which demonstrates stable p-type behavior.

The first p-type ZnO-NW-based piezotronic transistors were then developed, which extends the concept of piezotronics and its potential applications in the fields of flexible electronics and optoelectronics. *I–V* characteristics of the as-fabricated two-terminal device was obtained when the device was subject to different strains and corresponding results shown in Fig. 13a indicate that transport properties of the devices can be modulated by the applied mechanical strain. The polarity of the applied bias is with respect to the drain electrode. For a positive drain bias, the current through the device increased under tensile strain and decreased with compressive strain. Conversely, under a negative drain bias, the opposite trend was observed, with the current increasing under compressive strain and decreasing with increased tension. The 'gating' effect of external strain on charge-carrier transport in p-type ZnO NW piezotronic devices is demonstrated more explicitly in the inset of Fig. 13a. The corresponding strain-induced change in the SBH was calculated and plotted in the inset of Fig. 13a, demonstrating a change of 53 meV in the SBH at the drain contact with an applied compressive strain of 0.68%. The band diagrams of the p-type ZnO NW piezotronic device are shown in Fig. 13b to better explain the underlying working mechanism. Band diagrams shown here are for the positive drain bias, and corresponding diagrams can be obtained for the negative drain bias. The Schottky barrier at the metal/p-type semiconductor interface causes the band structure to bend downwards. For the case of the positive drain bias (Fig. 13b), the drain contact is reversely biased, so $\Delta\Phi_d$ dictates the charge-carrier transport. When tensile strain is applied to the device, due to the orientation of the *c*-axis of the p-type NW, negative piezoelectric polarization charges are induced at the drain contact. If the doping level inside the NW is finite, these immobile ionic charges will only be partially screened and can attract the majority of charge carriers, holes, toward the M–S interface that decreases the SBH at the drain contact ($\Phi'_d < \Phi_d$). At the same time, positive piezoelectric polarization charges are induced at the source contact, which results in an increased SBH at the source

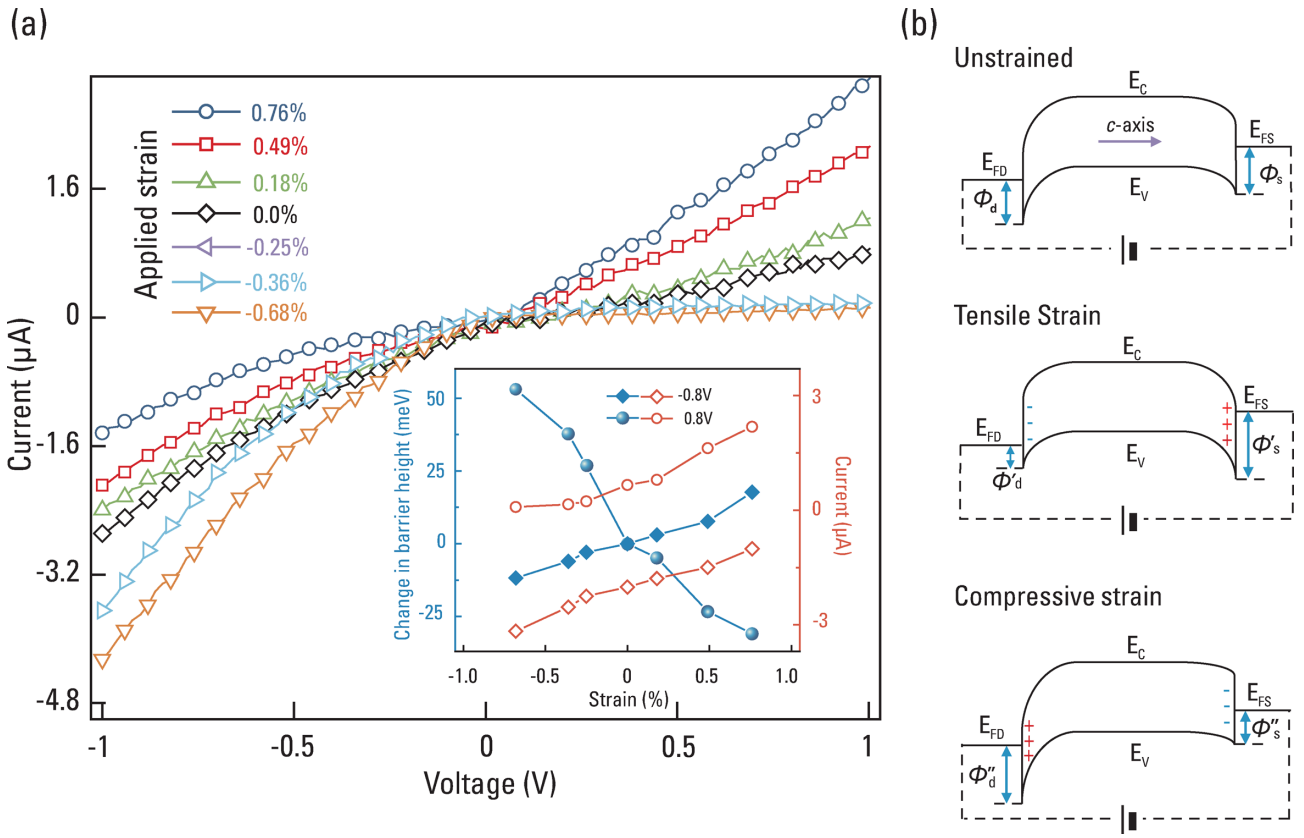

Figure 13. Observation of the piezotronic effect in a 0.2% Sb-doped NW. (a) *I–V* curves of the wire under different levels of strain show the modulation of device conductivity by mechanical strain. The inset shows the measured current and calculated change in the SBH as a function of strain at two fixed drain biases. (b) Positive drain bias on the NW causes the source and drain quasi-Fermi levels (E_{FS} and E_{FD}) to shift based on the level of the applied voltage. Tensile strain will induce negative piezoelectric polarization charges (blue '–') near the interface of the drain contact, attracting free holes, lowering the local SBH, and increasing current. Compressive strain will induce positive piezoelectric polarization charges (red '+') near the interface of the drain contact, depleting free holes, increasing the local SBH, and decreasing current [33] (Copyright 2013 American Chemical Society).

contact ($\Phi'_s > \Phi_s$). When compressive strain is applied to the device, on the other hand, positive piezoelectric polarization charges are induced at the drain contact, which depletes holes near the M–S interface and increases the SBH at the drain contact ($\Phi''_d > \Phi_d$). Simultaneously, negative piezoelectric polarization charges are induced at the source contact, lowering the SBH at the source contact ($\Phi''_s < \Phi_s$).

PIEZO-PHOTOTRONIC EFFECT AND PIEZO-PHOTOTRONICS

Piezo-phototronic effect

When light illumination is taken into account, the coupling among piezoelectricity, semiconductor behavior, and photon excitation characteristics of piezoelectric semiconductors can give rise to novel effect and applications. The presence of the localized piezoelectric polarization charges can significantly modulate/control the charge-carrier generation, separation, transport, and/or recombination at an interface/junction for achieving superior optoelectronic processes. This is the piezo-phototronic effect [10,11] that can significantly affect the performances of the LED, photodetector, and solar cell fabricated using these materials [46,84,85]. Devices fabricated by using the inner-crystal piezopotential as a 'gate' voltage to tune/control the above processes at the vicinity of a p–n junction is piezo-phototronics.

Basic theory of piezo-phototronics

Electrostatic equations, current-density equations, continuity equations, and piezoelectric equations are applied as basic governing equations for characterizing piezo-phototronic devices [86]. The following section attempts to establish the theoretic frame of piezo-phototronics by addressing the

fundamental piezo-phototronic effect in several typical optoelectronic devices.

Analytical solution for piezo-phototronic effect in solar cells

The basic structure of an NW solar cell is based on a p–n junction or M–S contact. The working principle of the solar cell is to use the large electric field in the depletion region to assist the separation of electron–hole pairs generated by incident photons. The piezoelectric polarization charges created at the junction under strain can significantly modify the band structure at the interface, resulting in a control over the carrier generation, separation, and transport at the p–n junction or the M–S interface and thus effectively tune/control the solar cell performance.

The analytical results for the ZnO piezoelectric p–n junction solar cell under simplified conditions have been obtained [84]. The current density of the p–n junction has been obtained in the section entitled 'Piezotronic effect in p–n junctions' with the presence of piezoelectric polarization charges. Taking into account the photocurrent density $J_{\rm solar}$, the total current density in the solar cell with piezopotential is

$$J = J_{\rm pn0}\cdot\exp[-q^2\rho_{\rm piezo}W_{\rm piezo}^2\cdot(2kT\varepsilon_{\rm s})^{-1}]\cdot[\exp(qV\cdot k^{-1}\cdot T^{-1})-1]-J_{\rm solar},$$

and the saturation current density with piezopotential is

$$J_{\rm pn} = J_{\rm pn0}\cdot\exp[-q^2\rho_{\rm piezo}W_{\rm piezo}^2\cdot(2kT\varepsilon_{\rm s})^{-1}],$$

assuming that the p-type side has an abrupt junction with a donor concentration, where $J_{\rm pn0} = qD_{\rm n}n_{\rm p0}\cdot L_{\rm n}^{-1}\cdot\exp[(E_{F0}-E_i)\cdot(kT)^{-1}]$ and $E_{\rm F0}$ are the saturation current density and Fermi level with the absence of piezopotential. $D_{\rm n}$ is the diffusion coefficient for electrons. $n_{\rm p0}$ is the thermal equilibrium electron concentration in a p-type semiconductor [84]. By setting $J = 0$, the open circuit voltage of the piezoelectric p–n junction solar cell is obtained as $V_{\rm oc} = kT\cdot q^{-1}\cdot\ln(J_{\rm solar}\cdot J_{\rm pn}^{-1}+1)$. For a typical solar cell condition $J_{\rm solar}\gg J_{\rm pn}$, the open circuit voltage can then be approximately as

$$V_{\rm oc}\approx kT\cdot q^{-1}\cdot\ln(J_{\rm solar}\cdot J_{\rm pn}^{-1}) = kT\cdot q^{-1}\cdot[\ln(J_{\rm solar}\cdot J_{\rm pn0}^{-1})+q^2\rho_{\rm piezo}W_{\rm piezo}^2\cdot(2kT\varepsilon_{\rm s})^{-1}].$$

The open circuit voltage can be effectively tuned not only by the magnitude of the strain, but also by the polarity of the strain. Though the above results are given by using a 1D NW model, it is expected that the mechanism of the piezo-phototronic effect can also be applied to bulk and thin-film solar cells. Similar discussions have also been applied to obtain analytical results for a ZnO piezoelectric Schottky-contact solar cell. The saturation current density $J_{\rm MS} = J_{\rm MS0}\cdot\exp(q^2\rho_{\rm piezo}W_{\rm piezo}^2\cdot(2kT\varepsilon_{\rm s})^{-1})$, in which the saturation current density with the absence of piezoelectric charges

$$J_{\rm MS0} = q^2D_{\rm n}N_{\rm C}\cdot(kT)^{-1}\cdot\sqrt{[2qN_{\rm D}\cdot(\psi_{\rm bi0}-V)\cdot\varepsilon_{\rm s}]}\cdot\exp[-q\phi_{Bn0}\cdot(kT)^{-1}],$$

where $\psi_{\rm bi0}$ and ϕ_{Bn0} are the built-in potential and SBH, respectively, with the absence of piezoelectric charges [84]. Therefore, the open circuit voltage of a Schottky-barrier piezoelectric solar cell is

$$V_{\rm oc}\approx kT\cdot q^{-1}\cdot[\ln(J_{\rm solar}\cdot J_{\rm MS0}^{-1})-q^2\rho_{\rm piezo}W_{\rm piezo}^2\cdot(2kT\varepsilon_{\rm s})^{-1}].$$

Using the piezoelectric effect created by external stress, the above theoretical study not only provides the basic physics for understanding the characteristics of the solar cell, but also assists the design for solar cells with better performance [22].

Analytical solution for piezo-phototronic effect in photodetectors

For a piezo-phototronic photodetector, the measurement of the photon-induced current is an indication of the incident photon intensity. For the n-type single-Schottky-contact photodetector, photo-excitation can effectively reduce the SBH, while the local piezoelectric polarization charges can change the SBH by

$$\Delta\phi_{\rm n} = -q\cdot(2\varepsilon)^{-1}\rho_{\rm piezo}W_{\rm piezo}^2-kT\cdot q^{-1}\cdot\ln[(n_0+\Delta n)\cdot n_0^{-1}],$$

where n_0 and Δn are the original carrier concentration and the excess carrier concentration, respectively. The electron current density transported through the forward-biased Schottky contact is then

$$J_{\rm n} = J_{\rm n0}\cdot(n_0+\Delta n)\cdot n_0^{-1}\cdot\exp[q^2\rho_{\rm piezo}W_{\rm piezo}^2\cdot(2kT\varepsilon_{\rm s})^{-1}],$$

where $J_{\rm n0}$ is the current density without applying light illumination or external strain [85]. As the sign of $\rho_{\rm piezo}$ depends on the direction of the *c*-axis and the polarity of the applied strain, the influence of piezoelectric charges can either enhance or reduce photo-excitation. For the n-type double-Schottky-contact photodetector with contacts 1 and 2, the

electron current density

$$J = J_{sv} \cdot \exp[-q\phi_{n0} \cdot (akT)^{-1}] \cdot \exp[Vqc \cdot (1 - a^{-1}) \cdot (kT)^{-1}] \cdot (n_0 + \Delta n) \cdot n_0^{-1} \cdot \exp[q^2 \rho_{piezo} W_{piezo}^2 \cdot (2akT\varepsilon)^{-1}],$$

where J_{sv} is the slowly varying term regarding the applied voltage and Schottky-barrier change, $a > 1$ and $c < 1$ are the two constants. Therefore, the current for Schottky contacts under different voltage biases takes the form

$$I = S_1 J_{C1} \cdot (n_0 + \Delta n) \cdot n_0^{-1/a} \cdot \exp[q^2 \rho_{piezo} W_{piezo}^2 \cdot (2akT\varepsilon)^{-1}]$$

when contact 1 is under the reverse bias ($V > 0$) and

$$I = -S_2 J_{C2} \cdot (n_0 + \Delta n) \cdot n_0^{-1/a} \cdot \exp[q^2 \rho_{piezo} W_{piezo}^2 \cdot (2akT\varepsilon)^{-1}]$$

when contact 2 is under the reverse bias ($V < 0$). Here, $J_{C1} = J_{sv1} \cdot \exp[-q\phi_{n10} \cdot (a_1 kT)^{-1}] \cdot \exp[Vqc_1 \cdot (kT)^{-1} \cdot (1 - a_1^{-1})]$ and $J_{C2} = J_{sv2} \cdot \exp[-q\phi_{n20} \cdot (a_2 kT)^{-1}] \cdot \exp[Vqc_2 \cdot (kT)^{-1} \cdot (1 - a_2^{-1})]$ are the reverse-biased current for contacts 1 and 2. S_1 and S_2 are the areas for contact 1 and contact 2, respectively. As $\rho_{piezo\,1}$ and $\rho_{piezo\,2}$ have opposite signs, the above results present the asymmetric change in photocurrent under the opposite bias by applying the same strain in the photodetectors.

Analytical solution for piezo-phototronic effect in LEDs

Based on the discussion in the section entitled 'Piezotronic effect in p–n junctions', the total current density for the piezotronic p–n junction is

$$J = J_{C0} \cdot \exp[q^2 \rho_{piezo} W_{piezo}^2 (2kT\varepsilon_s)^{-1}] \cdot \exp[qV \cdot (kT)^{-1} - 1].$$

Therefore, the optical power output for a piezoelectric LED can be obtained as

$$P_{optic} = \beta\{J_{C0} \cdot \exp[q^2 \rho_{piezo} W_{piezo}^2 (2kT\varepsilon_s)^{-1}] \cdot \exp[qV \cdot (kT)^{-1} - 1]\}^b,$$

where β is a constant depending on device materials and structures, b is the power-law parameter, with $b = 1$ corresponding to the linear approximation and $b \neq 1$ to the nonlinear approximation [86]. For a piezotronic p–n junction LED, the external quantum efficiency (EQE) with the presence of piezoelectric charges can be derived as $\eta_{ex} = \alpha\eta_{ex0}$, where η_{ex0} is the EQE without piezoelectric charges inside the p–n junction and the term representing the piezo-phototronic effect is $\alpha = \{\exp[q^2 \rho_{piezo} W_{piezo}^2 (2kT\varepsilon_s)^{-1}]\}^{b-1}$, which describes the modulation/tuning effect of piezoelectric charges on the carrier transport and photon recombination processes. More specifically, for a GaN or a ZnO NW grown along the *c*-axis, with a strain s_{33} along the *c*-axis, if a typical nonlinear approximation is chosen for $b = 2$, the optical power output for the corresponding piezotronic LED is given by $P_{optic} = \beta\{J_{C0} \cdot \exp[-qe_{33}s_{33}W_{piezo}(2kT\varepsilon_s)^{-1}] \cdot \exp[qV \cdot (kT)^{-1} - 1]\}^2$, and the EQE is $\eta_{ex} = \exp[-qe_{33}s_{33}\rho_{piezo}W_{piezo}(2kT\varepsilon_s)^{-1}] \cdot \eta_{ex0}$, which clearly demonstrates the tune/control of piezopotential on the photo-emission process in the piezotronic LED. This is the core physics of the piezo-phototronic effect.

More sophisticated theories can be developed for quantifying the observed piezo-phototronic phenomena, based on the above theoretical frame of piezo-phototronics for applications of the solar cell, photodetector, and LED. These analytical results have also been experimentally verified, as shown in the following sections.

PIEZO-PHOTOTRONIC EFFECT AND PIEZO-PHOTOTRONICS IN OPTOELECTRONIC APPLICATIONS

Piezo-phototronic effect on a solar cell

A solar cell is one of the most important optoelectronic applications. Using the barrier structure at the M–S interface and the internal field formed at the charge depletion zone at a p–n junction, photon-generated electron–hole pairs in the semiconductor materials are separated, giving rise to the electricity output. As shown in the previous sections, the presence of piezoelectric charges at the interface/junction can effectively modulate the charge separation, which is important for the solar cell efficiency. Experimental results consistent with the previous analytical discussions on the piezo-phototronic effect in solar cells have recently been demonstrated in an inorganic/organic solar cell made of poly(3-hexylthiophene) (P3HT)–ZnO microwire/NW [87], an n-CdS/p-Cu_2S coaxial NW-based solar cell [81], and quantum-dot-based solar cells [88].

For the P3HT–ZnO NW p–n heterojunction solar cell, V_{oc} increases and decreases with increasing the compressive strain and tensile strain, respectively, while I_{sc} almost shows a constant value of 0.035 nA under different strains [87]. When –0.35% strain is applied on the device, the V_{oc} can be enhanced by 38%, as compared to that without

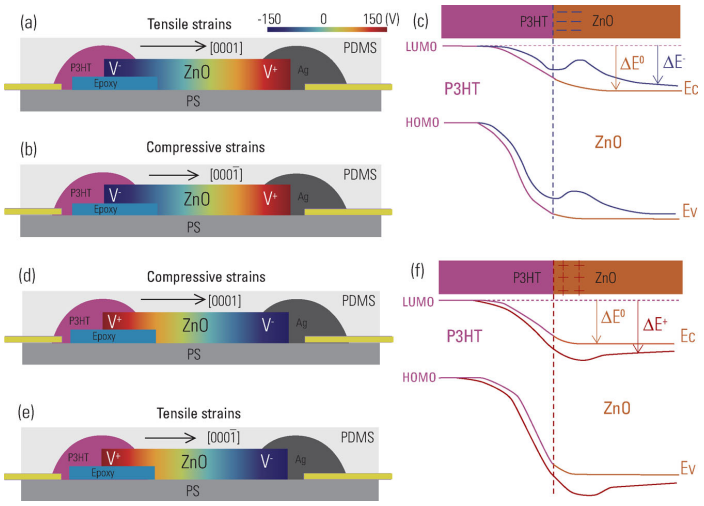

Figure 14. (a,b) The piezopotential distributions in the stretched device of [0 0 0 1] type and compressed device of [0 0 0 $\bar{1}$] type. (c) Schematic energy-band diagram of P3HT/ZnO with the presence of negative piezoelectric charges. The blue line indicates the modified energy-band diagram by the piezoelectric potential in ZnO. The negative piezoelectric charges can lift up the energy band, resulting in a peak in the energy band. (d,e) Calculated piezopotential distributions in the compressed device of [0 0 0 1] type and stretched device of [0 0 0 1] type. (f) Schematic energy-band diagram of P3HT/ZnO with the presence of positive piezoelectric charges. The red line represents the modified energy-band diagram of ZnO under compressive strain [87] (Copyright 2011 American Chemical Society).

strain. Two opposite change trends of V_{oc} with applied strains have been observed in the experiments, which can be attributed to the two contact configurations between the P3HT and ZnO NW and the corresponding distributions of piezopotential. In the first case, the direction from P3HT to ZnO is along [0 0 0 1], while in the other case the direction from P3HT to ZnO is along [0 0 0 $\bar{1}$]. The distribution of piezopotential in a single ZnO wire with the growth direction of [0 0 0 1] or [0 0 0 $\bar{1}$] can then be calculated by using the Lippmann theory [27] (Fig. 14). Although the calculated piezopotential at the end of the ZnO wire is up to 150 V, the actual piezopotential in ZnO is much lower due to the screening effect of the free-charge carriers. Considering the fact that P3HT is only in contact with the top side of the wire, when the device of the [0 0 0 1] type is under the tensile strain (Fig. 14a) or the device of the [0 0 0 $\bar{1}$] type is under compressive strains (Fig. 14b), the negative piezopotential is in contact with the P3HT, which lifts the local conduction band level of ZnO and results in a decrease of ΔE and V_{oc} (Fig. 14c). On the other hand, the positive piezoelectric polarization charges at the interface can lower the local conduction band level of ZnO, resulting in an increase of ΔE and V_{oc} (Fig. 14f). It has been reported that the tensile strain in the single ZnO NW along the [0 0 0 1] direction can decrease the bandgap of ZnO, which could increase the ΔE and the V_{oc}. However, since the piezoresistive effect is a non-polar and symmetric effect, it can only result in a similar trend of change in V_{oc} for the fabricated devices of [0 0 0 1] and [0 0 0 $\bar{1}$] types, which cannot explain the experimental results presented above.

The application of the piezo-phototronic effect in enhancing the solar cell performance has also been demonstrated using an n-CdS/p-Cu_2S coaxial NW-based solar cell [81]. Due to the polarity of the CdS NW growth direction, there are two different configurations of CdS/Cu_2S NW devices when the *c*-axis of the CdS NW pointing upward: one is the Cu_2S shell only located at the upper part of the CdS NW, denoted as configuration I (Fig. 15d); and the other is the Cu_2S shell only located at the lower part of the CdS NW, denoted as configuration II (Fig. 15g). The performance of the device with configuration I is enhanced when it is subjected to compressive strain up to –0.41%, and the I_{sc} is increased from 0.25 to 0.33 nA, while the V_{oc} varied between 0.26 and 0.29 V. The efficiency increased by ~70% when –0.41% compressive strain was applied. On the other hand, the performance of the device with configuration II dropped when the applied compressive strain was increased. The I_{sc} under different strains dropped from 3.47 to 3.05 nA, while the V_{oc} varied between 532 and 545 mV. CdS also has a non-central symmetric wurtzite structure, in which the cations and anions are tetrahedrally coordinated. Straining on the basic unit results in the polarization of the cations and anions and the piezopotential inside the crystal. For a coaxial n-CdS/p-Cu_2S NW solar cell, the performance is mainly determined by the carrier separation, transport, and recombination processes. Since the heavily doped p-Cu_2S shell is non-piezoelectric and is only 10–15 nm, the discussions are mainly focused on the piezoelectric CdS core. For the device with configuration I, the local positive piezoelectric charges at the Cu_2S/CdS interface (Fig. 15e) will lower the conduction and valence bands of CdS, as labeled in Fig. 15f, resulting in a decrease of the barrier height at the heterojunction interface. This is equivalent to increase the depletion width and internal field which will accelerate the separation of the electron–hole pair and reduce the possibility of recombination, thus enhancing the solar cell performance. For the device with configuration II, the effect of the local negative piezopotential at the Cu_2S/CdS interface (Fig. 15h) will lift up the conduction and valence bands of CdS, as labeled in Fig. 15i, resulting in an increase of the barrier height at the heterojunction interface. This is equivalent to decrease the depletion width and internal field which will make the electron–hole pair more difficult to be separated and thus increase the possibility of recombination. Subsequently, the output current and the

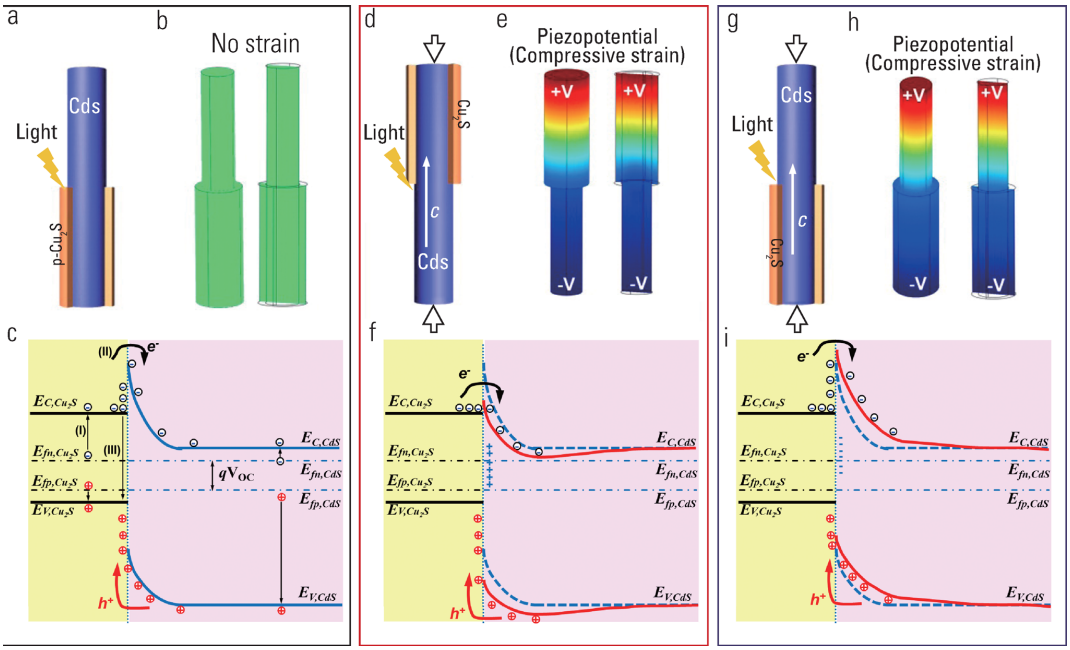

Figure 15. Schematics and energy-band diagrams demonstrate the piezo-phototronic effect on coaxial piezoelectric NW solar cells. (a–c) Numerically calculated piezopotential distribution and the corresponding energy-band diagram of a strain-free coaxial piezoelectric NW solar cell. (d,e) Numerically calculated piezopotential distribution and the corresponding energy-band diagram of a coaxial piezoelectric NW solar cell under compressive strain for a PV device with configuration. The upper part of the CdS NW is positively charged, while the lower part is negatively charged due to the piezoelectric potential under compressive strain. The positive charges at the CdS side lower the conduction and valence bands of CdS at the interface of the p–n junction that decreases the barrier height at the interface of the heterojunction, resulting in an enhancement of the PV performance. (g–i) Numerically calculated piezopotential distribution and the corresponding energy-band diagram of a coaxial piezoelectric NW solar cell under compressive strain for a PV device with configuration II. The negative charges at the CdS/Cu_2S interface lift up the conduction and valence band of CdS at the interface of the p–n junction, thus resulting in a drop of the PV device [81] (Copyright 2012 American Chemical Society).

convention efficiency are decreased when the device is compressively strained.

Colloidal quantum-dot solar cell (QDSC) is also a promising candidate for effective solar energy harvesting. Recently, a novel strategy to modulate the interfacial band structure of ZnO/PbS QDSCs by piezoelectric polarization (P_{pz}) has been presented [88]. The enhancement of the J_{sc} and efficiency was mostly due to the extension of the depletion region in PbS by the P_{pz}-induced charge redistribution at the ZnO/PbS interface. The change of the V_{oc} was less significant and consisted of two components: photocurrent-related quasi-Fermi level shifting and the remnant piezopotential at the ZnO/ITO interface. The solar cell performance became less responsive to P_{pz} under higher illumination intensity due to the compensation from trapped photo-excited charges at the interface.

Piezo-phototronic effect on a photodetector

The operation of a photodetector is based on the separation of photon-generated electron–hole pairs by either a p–n junction or a Schottky barrier. In Schottky-barrier-based photodetectors, the SBH is therefore important for dictating the detection sensitivity. By tuning the SBH in a ZnO-wire-based UV sensor, which possesses the metal–semiconductor–metal (MSM) structure, through applying a strain, it has been demonstrated that the sensitivity of the UV detector can be significantly improved, especially when the illumination intensity is rather weak [82]. The responsivity of the photodetector is enhanced by 530%, 190%, 9%, and 15% upon the UV light illumination of 0.75 μW cm^{-2}, 22 μW cm^{-2}, 0.75 mW cm^{-2}, and 33 mW cm^{-2}, respectively, when the ZnO NW experiences –0.36% compressive strain. The sensitivity for weak-light illumination is significantly enhanced by introducing the strain, although the strain almost has little effect on the sensitivity to stronger light illumination. The effect of piezopotential decreases with increasing light intensity, which may be due to the fact that newly generated charge carriers will accumulate and partially screen the piezopotential. On the other hand, the surface of the ZnO NW in the dark is depleted by the absorbed oxygen molecules and the dark

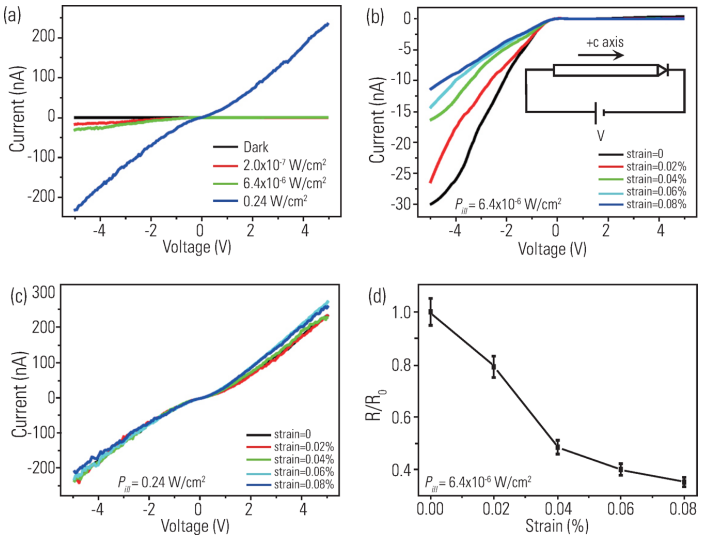

Figure 16. Experimental results for a CdS NW MSM photodetector with a single Schottky contact. Light illumination with monochromic blue light centered at 486 nm. (a) Current–voltage characteristic under different illumination power. The inset shows the dark current without strain. (b) Current–voltage characteristic under different strain when the illumination power is 6.4×10^{-6} W cm^{-2}. Inset is the configuration of the device and the direction of the forward bias. (c) Current–voltage characteristic under different strains when the illumination power is 0.24 W cm^{-2}. (d) Calculated relative responsivity under various applied strain when the illumination power is 6.4×10^{-6} W cm^{-2} [85] (Copyright 2012 WILEY-VCH, Weinheim).

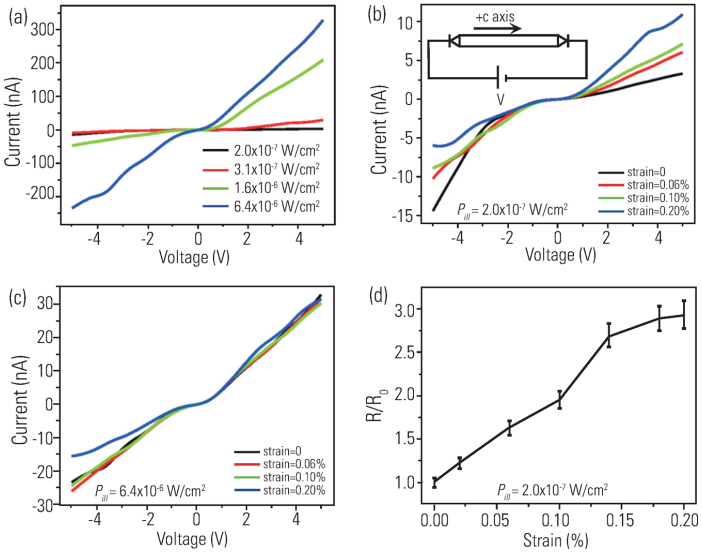

Figure 17. Experimental results for a CdS nanowire MSM photodetector with double Schottky contacts. Light illumination with monochromic blue light centered at 486 nm. (a) Current–voltage characteristic under different illumination power. (b) Current–voltage characteristic under different strain when the illumination power is 2.0×10^{-7} W cm^{-2}. Inset is the configuration of the device and the direction of the forward bias. Inset is the configuration of the device and the direction of the forward bias. (c) Current–voltage characteristic under different strains when the illumination power is 6.4×10^{-6} W cm^{-2}. (d) Calculated relative responsivity under various applied strain when the illumination power is 2.0×10^{-7} W cm^{-2}. R0 is set as responsivity under zero strain for this illumination power [85] (Copyright 2012 WILEY-VCH, Weinheim).

current is very low (~14 pA at the –5 V applied bias). In this case, the device can be considered as an insulator wire sandwiched between two back-to-back Schottky diodes, and the current is controlled by the bulk of the sample not by the Schottky contact. Thus, although piezopotential can modulate the SBH, it has little effect on the dark current. Consequently, piezopotential dramatically increases the responsivity for pW level light detection, while keeps low dark current characteristics of the devices, which is beneficial for the low-intensity light detection. Our results show that the piezo-phototronic effect can enhance the detection sensitivity more than five-fold for pW level light detection [82].

Recently, theoretical efforts have been made to couple the photo-excitation and piezoelectric terms into basic current equations to study their influence on the operation of the photodetector. The theoretically predicted results have also been quantitatively verified by photodetectors based on ZnO NWs for UV light and CdS NWs for visible light [85]. Two kinds of typical MSM photodetectors, single-Schottky-contact photodetector and double-Schottky-contact photodetector, exist in the experiments. Fig. 16 is the result for a single-Schottky-contact photodetector in which the current decreases with increasing strain. In Fig. 16d, illumination power is kept at 6.4×10^{-6} W cm^{-2}, and the change of responsivity R with the applied strain for the photodetector is calculated. It can be seen that the responsivity in this case decreases with tensile strain. Fig. 17 is the result for a double-Schottky-contact photodetector. While the current under forward bias increases with the applied strain, under the reverse bias the current decreases with it. A similar modulation of sensitivity by mechanical strain has also been reported for photodetectors based on ZnO/CdS core/shell structures [79]. These experimental results show that the piezo-phototronic effect can effectively modulate the performance of photodetectors, which is significantly pronounced at low light intensities, and is important for extending the sensitivity and application range of photodetectors. The conclusions drawn on Schottky contacts present the core of the effect and can easily be extended to other structures like p–n junctions.

Piezo-phototronic effect on LEDs

Light emission from semiconductors depends on the efficiency of carrier injection, recombination, and extraction. The piezo-phototronic effect has been utilized to effectively enhance the external efficiency of an LED fabricated using a single ZnO NW on a GaN substrate [46]. At a fixed applied bias above

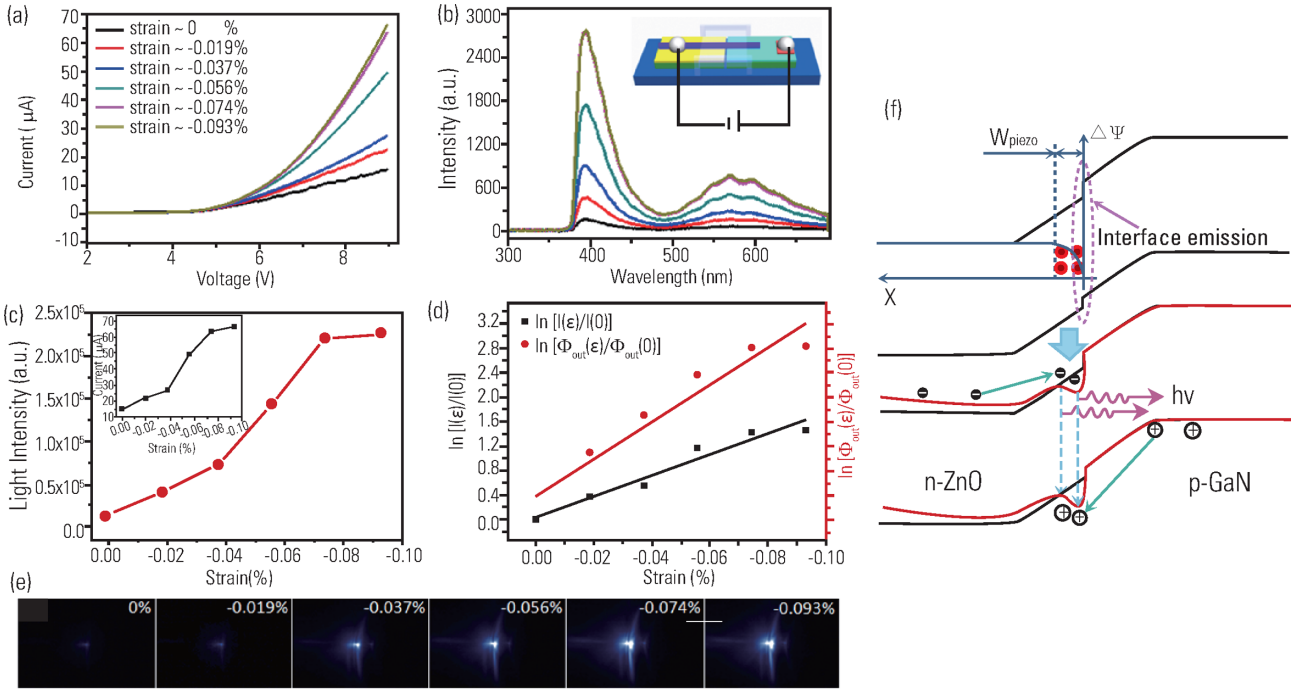

Figure 18. Enhancement of light emission intensity and conversion efficiency of an (n-ZnO wire)–(p-GaN film) LED under the applied strain. A schematic diagram of the fabricated device. (a) *I–V* characteristics of the device at the forward bias with the variation of the applied strain; and (b) the corresponding optical spectra of the emitted light at a bias of 9 V. (c) Integrated light emission intensities from the data shown in (b), showing a huge increase in the emission intensity with the increase of the applied compressive strain. The inset is the injection current of the LED at 9 V biasing voltage with the increase of the strain. (d) Change in relative injection current and relative light emission intensity under different strain. The LED efficiency has been increased by a factor of 4.25 at the maximum applied strain in comparison to the zero strain case. (e) CCD images recorded from the emitting end of a packaged single wire LED under different applied strain. (f) Schematic energy-band diagram of the p–n junction without (upper) and with (lower, red line) applied compressive strain, where the channel created at the interface inside ZnO is due to the piezopotential created by strain [42] (Copyright 2011 American Chemical Society).

the turn-on voltage (3 V), the current and light emission intensity increased obviously with the increase of the compressive strain (Fig. 18a and b). The significantly enhanced light intensity can be directly observed in optical images (Fig. 18e). The $\ln[I(\varepsilon)/I(0)]$ and $\ln[\phi_{out}(\varepsilon)/\phi_{out}(0)]$ dependence on strain ε is shown in Fig. 18d, where $\phi_{out}(\varepsilon)$ and $I(\varepsilon)$ are the light intensity and the injection current of the LED under strain, respectively; and $\phi_{out}(0)$ and $I(0)$ are the corresponding quantities of the as-fabricated LED without applying an external strain; both curves have a linear relationship with the external strain, and the slope of $\ln[\phi_{out}(\varepsilon)/\phi_{out}(0)]$–$\varepsilon$ is larger than that of $\ln[I(\varepsilon)/I(0)]$–ε, indicating a clear increase in light-conversion efficiency. The injection current and output light intensity were largely enhanced by a factor of 4 and 17, respectively, after applying 0.093% *a*-axis compressive strain, indicating that the conversion efficiency was improved by a factor of 4.25 in reference to that without applying strain. This means that the external efficiency of the LED can reach ~7.82% after applying strain, which is comparable to that of the LED structures based on nanorods hybrid quantum-well LED. As for the ZnO (n-type)–GaN (p-type) LED, a schematic diagram of its band structure is presented in Fig. 18f. The finite doping in the wire may partially screen the piezoelectric charges and a dip in the band is possible. If the *c*-axis of the ZnO wire is pointing from the ITO side to the GaN side, the effect of the local negative piezopotential at the ITO side is equivalent to applying an extra forward-biased voltage on the device. Thus, the depletion width and internal field are reduced under this additional component of forward-biased voltage. Subsequently, the injection current and emitting light intensity under the same externally applied forward voltage increase when the device is strained. Alternatively, if the *c*-axis of the ZnO wire is reversed and pointing away from the GaN side, the GaN side has a lower piezopotential, which is equivalent to applying an extra reverse-biased voltage on the device. The depletion width and internal field are thus increased, resulting in a reduction of the injection current and light emission intensity with the increase of the applied strain.

Organic/inorganic hybridized UV LEDs based on ZnO nanostructures have shown very low EQEs due to the difficulties in achieving the current

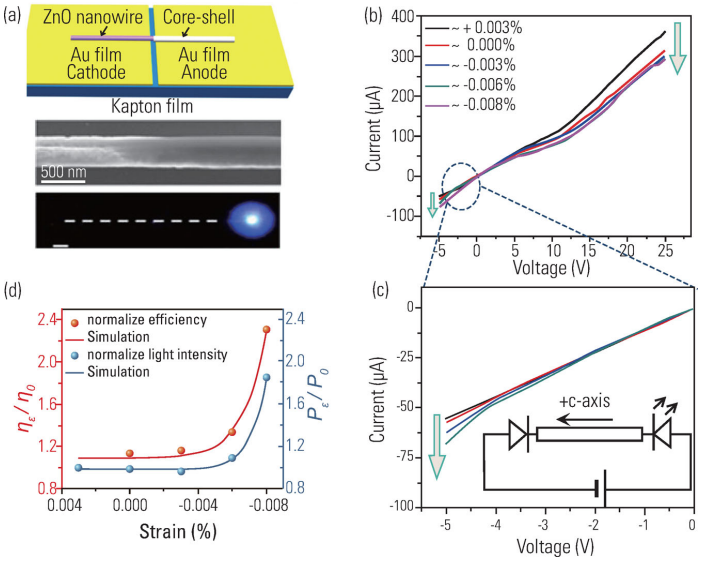

Figure 19. (a) Schematic diagram and SEM image of a ZnO NW/PEDOT:PSS core shell structure. The bottom is the CCD image of the LED at 25 V biasing voltage, and the dashed line represents the physical location of the ZnO NW/p-polymer core-shell structure. Scale bar is 10 μm. (b) *I–V* characteristics of the device at forward bias with the variation of the applied strain. (c) The enlarged picture of the *I–V* curve circled by the dashed line. Insets are the configuration of the device and direction of forward bias. (d) Change in relative light intensity P_ε/P_0 and external efficiency $\beta_\varepsilon/\beta_0$ under different strain [72] (Copyright 2013 American Chemical Society).

balance between electrons and holes as well as high non-radiative recombination induced by surface defects [89,90]. Recently, it has been reported that the piezo-phototronic effect can be utilized to effectively enhance the external efficiency of an inorganic/organic LED based on a single ZnO NW/p-polymer core-shell structure [78]. Under the fixed forward bias above the turn-on threshold voltage, the current decreases step by step when the applied strain varies from 0.003% tensile strain to –0.008% compressive strain. The asymmetric characteristic in the *I–V* curve at the negative and positive biases (Fig. 19d and e) indicates that the change is mainly due to the piezo-phototronic effect [85]. Corresponding theoretical simulation confirms that most of the electric field is localized in the *x*-direction (the axial direction of the NW) near the end polar surface of the NW where ZnO is in contact with PEDOT:PSS, which is also the area where piezoelectric charges are distributed. Experimental results confirmed that the light emission is localized near the end surface of the NW. The schematic band diagram of the device without strain shows that the barrier for hole injection from PEDOT:PSS into ZnO is high and makes the recombination being largely limited by hole injection and transport. The efficiency is low as the majority of electrons flow through without sufficient recombination with holes. When strain is applied to the device with a forward bias, the corresponding change in band profiles due to the piezoelectric effect can enhance the electron–hole recombination and efficiency significantly. If the *c*-axis of the ZnO NW is pointing away from the p-polymer and the ZnO NW is under compressive strain, the effect of the local negative piezopotential at the cathode will increase the SBH, while the local positive piezopotential near the p–n junction will introduce a carrier channel owing to a dip at the local band. Consequently, the light emission intensity and EQE of the hybrid LED have been enhanced to 190% and 230%, respectively, after applying –0.008% compressive strain when the *c*-axis of ZnO NW is pointing away from the p-polymer. Meanwhile, when the *c*-axis of the ZnO NW is pointing toward the p-polymer, the light emission intensity and EQE have been enhanced to 230% and 370%, respectively, after applying 0.017% tensile strain.

In addition, it is also reported that the electroluminescence (EL) properties of p-type GaN thin films can be tuned by the piezo-phototronic effect via adjusting minority carrier injection efficiency at the M–S interface by strain-induced polarization charges [80]. When strain was applied to the GaN film, the induced piezoelectric charges at the ITO/GaN interface modified the SBH, and two kinds of changing trends of the transport properties were obtained depending on the *c*-axis orientations of the GaN films. Also, these piezoelectric charges changed the minority carrier injection efficiency at the M–S interface, which resulted in a modification of the EL emission intensity. The EQE of the blue EL at 430 nm was changed by 5.84% under different straining conditions, which is one order of magnitude larger than the change of the green peak at 540 nm. The piezo-phototronic effect thus has a more pronounced effect on the EL emission process involving the shallow-acceptor states than the one involving the deep-acceptor states in the p-type GaN thin films. By eliminating the current change effect, the integral EL intensity was modulated by 2.11% for the emission at 430 nm, and 0.21% for the emission at 540 nm due to the piezo-phototronic effect under different straining conditions. As GaN is a dominant material for the optoelectronic devices, this study provides a further understanding for future applications of GaN in flexible optoelectronics. It is also demonstrated that photoluminescence (PL) properties of bent ZnO NWs can be modified by strain-induced piezoelectric polarization [91].

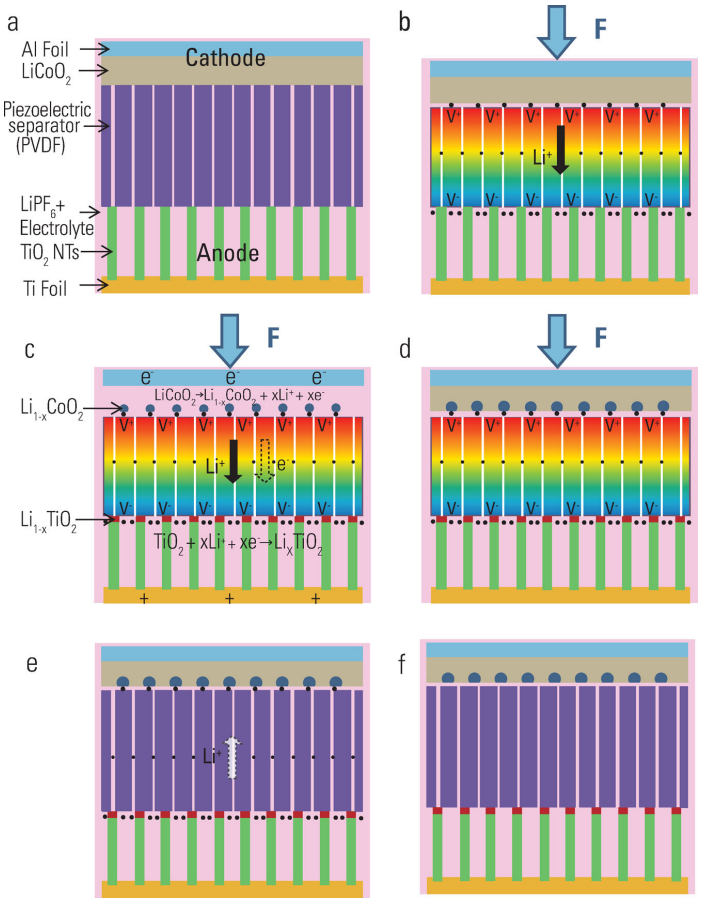

Figure 20. The working mechanism of the SCPC under compressive strains. (a) Schematic illustration of the SCPC in discharged state. (b) When compressive stress is applied onto the device, the piezoelectric separator layer creates a piezopotential, with the positive polarity at the cathode side and negative piezopotential at the anode side. (c) Under the driving of the piezoelectric field, the Li ions from the cathode migrate through the PVDF film separator in the electrolyte toward the anode, leading to the corresponding charging reactions at the two electrodes. (d) The status where chemical equilibrium of the two electrodes is re-established and the self-charging process ceases. (e) When the applied force is released, the piezoelectric field of the PVDF disappears that breaks the electrostatic equilibrium, so that a portion of the Li ions will diffuse back to the cathode. (f) A new equilibrium is reached and a cycle of self-charging is completed [85] (Copyright 2012 American Chemical Society).

EFFECT OF PIEZOPOTENTIAL IN ELECTROCHEMICAL PROCESSES AND ENERGY STORAGE

Effect of piezopotential in mechanical-to-electrochemical energy conversion

Electricity generation and energy storage have long been two different processes that are accomplished through separated physical units to achieve the conversions from mechanical energy to electric energy and then from electric energy to chemical energy. Recently, the direct conversion of mechanical energy into simultaneously stored chemical energy has been demonstrated by hybridizing the above two steps into one using a single hybridized structure [92]. Such an integrated self-charging power cell (SCPC), which can be charged up by mechanical deformation and vibration from the environment, provides an innovative approach for developing a new mobile power source for both self-powered systems and portable and personal electronics.

The working mechanism of the SCPC is an electrochemical process driven by deformation-induced piezopotential (Fig. 20). At the beginning, the device is at a discharged state, with $LiCoO_2$ as the positive electrode (cathode) material, TiO_2 nanotube as the negative electrode (anode), and the $LiPF_6$ electrolyte is evenly distributed across the entire space, as shown in Fig. 20a. A polyvinylidene difluoride (PVDF) film, which has intimate contacts with both electrodes, serves as the separator and it has the smallest Young's modules among all of the components in the device; thus, it experiences the largest compressive strain when a compressive stress is applied onto the device, as shown in Fig. 20b. The polarized PVDF film can result in a positive piezopotential at the cathode ($LiCoO_2$) side and negative piezopotential at the anode (TiO_2) under compressive strain for separating the charges. Under the driving of the piezopotential field with a direction from the cathode to the anode, the Li ions in the electrolyte will migrate along this direction through the ionic conduction paths present in the PVDF film separator in order to screen the piezopotential field, and finally reach the anode, as shown in Fig. 20c. The decreased concentration of Li^+ at the cathode will break the chemical equilibrium of the cathode electrode reaction ($LiCoO_2 \Leftrightarrow Li_{1-x}CoO_2 + xLi^+ + xe^-$), so that Li^+ will de-intercalate from $LiCoO_2$, turning it into $Li_{1-x}CoO_2$ and leaving free electrons at the current collector (Al foil) of the cathode electrode. Meanwhile, under the elevated concentration of Li^+ at the anode, the reaction at the other electrode ($TiO_2 + xLi^+ + xe^- \Leftrightarrow Li_xTiO_2$) will move to the forward direction for the same reason, enabling Li^+ to react with TiO_2, so that Li_xTiO_2 will be produced at the anode electrode, leaving the positive charges at the Ti foil. During this process, Li^+ will continuously migrate from the cathode to the anode, and the device is charged up a little bit owing to the large volume of the device. During the progress of charging electrochemical reactions at the two electrodes, extra free electrons will transfer from the cathode to the anode in order to maintain the charge neutrality and the continuity of the charging reaction. In the second step, when the applied force is released, the piezoelectric field inside the PVDF disappears, which breaks the electrostatic equilibrium. Therefore, a portion of the Li ions diffuse back

from the anode to the cathode (Fig. 20e) and reach an even distribution of Li^+ all over the space in the device again (Fig. 20f). Then, a cycle of charging is completed through an electrochemical process of oxidizing a small amount of $LiCoO_2$ at the cathode to $Li_{1-x}CoO_2$ and reducing a bit of TiO_2 to Li_xTiO_2 at the anode. When the device is mechanically deformed again, the process presented above is repeated, resulting in another cycle of charging by converting mechanical energy directly into chemical energy. Under the compressive force applied to the SCPC at a frequency of 2.3 Hz, the voltage of the device increased from 327 to 395 mV in 240 s. After the self-charging process, the device was discharged back to its original voltage of 327 mV under a discharge current of 1 μA, which lasted for ~130 s. The proposed power cell can be charged up under the repeated deformation by directly converting mechanical energy to chemical energy. In this experimental case, the stored electric capacity of the power cell was ~0.036 μAh.

By replacing the polyethylene separator as for the conventional Li battery with a piezoelectric PVDF film, the piezopotential induced inside the PVDF film under straining acts as a charge pump to drive Li ions migrate from the cathode to the anode accompanying with charging reactions at electrodes, which can be defined as a piezo-electrochemical process and provides an innovative approach for developing new energy technology for driving personal electronics and self-powered systems.

Piezo-phototronic effect on photoelectrochemical processes

A photoelectrochemical (PEC) process is the fundamental of photon–water splitting and energy storages. The efficiency of PEC is dictated by the charge generation and separation processes. A typical PEC system is made of an n-type semiconductor that is in direct contact with an electrolyte. A natural Schottky barrier of height ϕ_B is present at the semiconductor–electrolyte interface. Once a photon with energy higher than the bandgap of the semiconductor illuminates at the interface, an electron–hole pair is generated. The excited electron tends to drift toward the semiconductor side in the conduction band owing to the inclined band, which then is transported through the external load to the electrode owing to a difference in Fermi levels at the two sides. The hole drifts toward the electrolyte. If the energy possessed by the hole is more than the oxidation potential, it can stimulate an oxidation process to cover an A species into A^+. The electron at the counter-electrode side is then recaptured by

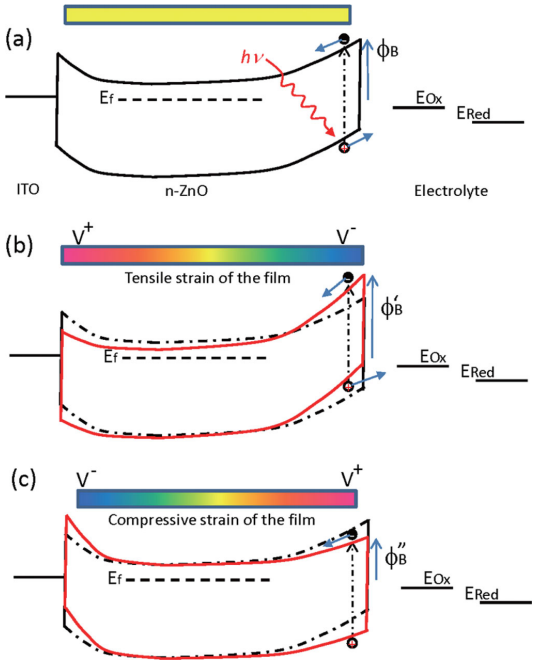

Figure 21. Effect of piezopotential in the semiconductor on the PEC process. (a) Band structure of the PEC with the absence of piezopotential. (b) Band structure of the PEC when the film is under tensile strain, so that the side directly interfacing with the electrolyte has a lower piezopotential. (c) Band structure of the PEC when the film is under compressive strain, so that the side directly interfacing with the electrolyte has a higher piezopotential [11] (Copyright 2013 Springer).

A^+ if the reduction potential is lower than the Fermi level of the electrode, so that it is reduced into A. In the state-of-the-art photocatalysis technologies, the manipulation of charge-carrier separation and transport is often achieved via introducing gradients of the electrical potential by external power supply and/or establishing electronic-state discontinuities by interface engineering [93–100].

For a piezoelectric semiconductor, if a tensile strain is applied to the semiconductor film, so that the side directly interfacing with the electrolyte has a lower piezopotential, the valence band edge is uplifted, so that it is close to the oxidation potential E_{Ox}, as shown in Fig. 21b; thus, the hole has enough energy to trigger the oxidation process. At the same time, the steeply raised conduction band at the electrolyte side accelerates the drift of the electron in the conduction band toward the ITO side. Furthermore, the valence band at the ZnO–ITO contact is lowered, reducing the local resistance or threshold voltage for electron transport. All of these processes are favorable for enhancing the efficiency of PEC. Alternatively, by applying compressive strain to the

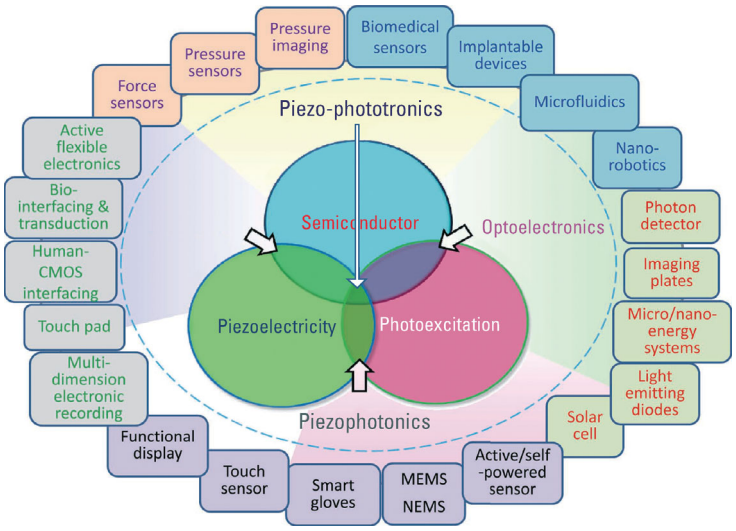

Figure 22. Schematic diagram showing the coupling among piezoelectricity, photo-excitation, and semiconducting property in piezoelectric semiconductor materials, which is the basis of piezotronics (piezoelectricity-semiconductor coupling), piezo-photonics (piezoelectric–photon excitation coupling), optoelectronics, and piezo-phototronics (piezoelectricity–semiconductor–photo-excitation). Many novel applications can be implemented by utilizing these processes and effects [10] (Copyright 2012 WILEY-VCH, Weinheim).

film, the local piezopotential at the electrolyte interface is high, as shown in Fig. 21c, and the lowered valance band reduces the energy of the hole, so that it may not be effective to stimulate the redox process or at least at a reduced efficiency. Furthermore, the flattered conduction band at the electrolyte side reduces the drift speed of the electron toward the ITO side. The raised conduction band at the ITO side increases the threshold voltage and the local resistance. All of these processes can largely reduce the efficiency of PEC. An enhancement or reduction of photocurrent in consistent with the above discussions was observed in recent reports when tensile or compressive strains were applied to the ZnO anode in the PEC, respectively [93,101,102]. The photocurrent variations in these reports are attributed to a change in barrier height at the ZnO/electrolyte interface by strain-induced piezopotential.

OUTLOOK AND SUMMARY

The rapid advancement in micro/nanotechnology nowadays will gradually shift its focus from demonstrating discrete devices to developing integrated system of certain complexity, which is capable of performing multi-functions, such as sensing, actuating/responding, communicating, and controlling by integrating individual devices via state-of-the-art microfabrication technologies. Due to the gigantic difference in materials systems, conventionally the research overlap between piezoelectricity and electronics/optoelectronics has been rather limited. Based on piezoelectric semiconductor materials, such as ZnO, GaN, and InN, a few new research fields have been proposed and developed by coupling piezoelectricity with the semiconductor and photo-excitation properties (Fig. 22) [10]. The core of these emerging research and applications relies on strain-induced piezopotential that is generated by the polarization of ions in the crystal. Piezotronics is the family of devices fabricated using the piezopotential as a 'gate' voltage to tune/control charge-carrier transport at a contact or junction. Piezo-phototronic effect utilizes the piezopotential to control the carrier generation, transport, separation, and/or recombination for improving the performance of optoelectronic devices. Piezotronics and piezo-phototronics are expected to have important applications in sensors, bio-integrated systems, human–machine interfacing, MEMS, energy sciences, and integration with silicon-based CMOS technology for achieving augmented functionalities in the era of 'More Than Moore' [103].

ACKNOWLEDGEMENTS

The authors thank the support of National Science Foundation, Defense Advanced Research Projects Agency, National Institute of Health and Chinese Academy of Sciences. We sincerely thank the following colleagues who made significant contributions to the work presented here (not in particular order): Jun Zhou, Youfan Hu, Xudong Wang, Qing Yang, Yan Zhang, Ying Liu, Caofeng Pan, Jr-Hau He, Yifan Gao, Xiaonan Wen, Weihua Han, Yusheng Zhou, and many others.

REFERENCES

1. Diamond, D, Coyle, S and Scarmagnani, S *et al.* Wireless sensor networks and chemo-/biosensing. *Chem Rev* 2008; **108**: 652–9.
2. Kim, S, Pakzad, S and Culler, D *et al.* Health monitoring of civil infrastructures using wireless sensor networks. In *Proceedings of the Sixth International Symposium on Information Processing in Sensor Networks, Cambridge, MA* 2007; 254–63.
3. Sanders, D. Environmental sensors and networks of sensors. *Sensor Rev* 2008; **28**: 273–4.
4. Hao, Y and Foster, R. Wireless body sensor networks for health-monitoring applications. *Physiol Meas* 2008; **29**: R27–R56.
5. Kim, DH, Ghaffari, R and Lu, NS *et al.* Flexible and stretchable electronics for biointegrated devices. *Annu Rev Biomed Eng* 2012; **14**: 113–28.
6. Alivisatos, AP, Andrews, AM and Boyden, ES *et al.* Nanotools for neuroscience and brain activity mapping. *ACS Nano* 2013; **7**: 1850–66.
7. Wang, ZL. Self-powered nanosensors and nanosystems. *Adv Mater* 2012; **24**: 280–5.
8. Wang, ZL. Toward self-powered sensor networks. *Nano Today* 2010; **5**: 512–4.

9. Wang, ZL and Wu, WZ. Nanotechnology-enabled energy harvesting for self-powered micro-/nanosystems. *Angew Chem Int Edit* 2012; **51**: 11700–21.
10. Wang, ZL. Progress in piezotronics and piezo-phototronics. *Adv Mater* 2012; **24**: 4632–46.
11. Wang, ZL. *Piezotronics and piezo-phototronics*. Berlin: Springer, 2013.
12. Gautschi, G. *Piezoelectric sensorics: force, strain, pressure, acceleration and acoustic emission sensors, materials and amplifiers*. Berlin: Springer, 2002.
13. Chen, H, Jia, C and Zhang, C *et al.* Power harvesting with PZT ceramics. *IEEE Int Symp Circ S* 2007; 557–60.
14. Tseng, KK and Wang, L. Smart piezoelectric transducers for in situ health monitoring of concrete. *Smart Mater Struct* 2004; **13**: 1017–24.
15. Izyumskaya, N, Alivov, Y and Cho, SJ *et al.* Processing, structure, properties, and applications of PZT thin films. *Crit Rev Solid State* 2007; **32**: 111–202.
16. Wang, ZL. Piezopotential gated nanowire devices: piezotronics and piezo-phototronics. *Nano Today* 2010; **5**: 540–52.
17. Wang, ZL. Towards self-powered nanosystems: from nanogenerators to nanopiezotronics. *Adv Funct Mater* 2008; **18**: 3553–67.
18. Wang, ZL, Yang, RS and Zhou, J *et al.* Lateral nanowire/nanobelt based nanogenerators, piezotronics and piezo-phototronics. *Mat Sci Eng R* 2010; **70**: 320–9.
19. Wang, ZL and Song, JH. Piezoelectric nanogenerators based on zinc oxide nanowire arrays. *Science* 2006; **312**: 242–6.
20. Zhou, J, Fei, P and Gu, YD *et al.* Piezoelectric-potential-control led polarity-reversible Schottky diodes and switches of ZnO wires. *Nano Lett* 2008; **8**: 3973–7.
21. Boxberg, F, Sondergaard, N and Xu, HQ. Elastic and piezoelectric properties of zincblende and wurtzite crystalline nanowire heterostructures. *Adv Mater* 2012; **24**: 4692–706.
22. Boxberg, F, Sondergaard, N and Xu, HQ. Photovoltaics with piezoelectric core-shell nanowires. *Nano Lett.* 2010; **10**: 1108–12.
23. Wang, XD, Song, JH and Liu, J *et al.* Direct-current nanogenerator driven by ultrasonic waves. *Science* 2007; **316**: 102–5.
24. Qin, Y, Wang, XD and Wang, ZL. Microfibre–nanowire hybrid structure for energy scavenging. *Nature* 2008; **451**: 809–13.
25. Wang, ZL. Nanopiezotronics. *Adv Mater* 2007; **19**: 889–92.
26. Song, JH, Xie, HZ and Wu, WZ *et al.* Robust optimization of the output voltage of nanogenerators by statistical design of experiments. *Nano Res* 2010; **3**: 613–9.
27. Gao, Y and Wang, ZL. Electrostatic potential in a bent piezoelectric nanowire. The fundamental theory of nanogenerator and nanopiezotronics. *Nano Lett* 2007; **7**: 2499–505.
28. Yang, SZ, Wang, LF and Tian, XZ *et al.* The piezotronic effect of zinc oxide nanowires studied by in situ TEM. *Adv Mater* 2012; **24**: 4676–82.
29. Gao, ZY, Zhou, J and Gu, YD *et al.* Effects of piezoelectric potential on the transport characteristics of metal-ZnO nanowire-metal field effect transistor. *J Appl Phys* 2009; **105**: 113707.
30. Schmidt-Mende, L and MacManus-Driscoll, JL. ZnO nanostructures, defects, and devices. *Mater Today* 2007; **10**: 40–8.
31. Gao, Y and Wang, ZL. Equilibrium potential of free charge carriers in a bent piezoelectric semiconductive nanowire. *Nano Lett* 2009; **9**: 1103–10.
32. Vetury, R, Zhang, NQQ and Keller, S *et al.* The impact of surface states on the DC and RF characteristics of A1 GaN/GaN $HFET_s$. *IEEE T Electron Dev* 2001; **48**: 560–6.
33. Lu, MP, Song, J and Lu, MY *et al.* Piezoelectric nanogenerator using p-type ZnO nanowire arrays. *Nano Lett* 2009; **9**: 1223–7.
34. Yuan, GD, Zhang, WJ and Jie, JS *et al.* P-type ZnO nanowire arrays. *Nano Lett* 2008; **8**: 2591–7.
35. Wang, F, Seo, JH and Bayerl, D *et al.* An aqueous solution-based doping strategy for large-scale synthesis of Sb-doped ZnOnanowires. *Nanotechnology* 2011; 22.
36. Pradel, KC, Wu, WZ and Zhou, YS *et al.* Piezotronic effect in solution-grown p-type ZnO nanowires and films. *Nano Lett* 2013.
37. Yankovich, AB, Puchala, B and Wang, F *et al.* Stable p-type conduction from Sb-decorated head-to-head basal plane inversion domain boundaries inZnO nanowires. *Nano Lett* 2012; **12**: 1311–6.
38. Wu, WZ, Wei, YG and Wang, ZL. Strain-gated piezotronic logic nanodevices. *Adv Mater* 2010; **22**: 4711–5.
39. Wu, WZ and Wang, ZL. Piezotronic nanowire-based resistive switches as programmable electromechanical memories. *Nano Lett* 2011; **11**: 2779–85.
40. Wang, ZL. From nanogenerators to piezotronics-a decade-long study of ZnO nanostructures. *MRS Bull* 2012; **37**: 814–27.
41. Tung, RT. Recent advances in Schottky barrier concepts. *Mat Sci Eng R* 2001; **35**: 1–138.
42. Rhoderick, EH and Williams, RH. *Metal-semiconductor contacts*. 2nd edn, Oxford: Clarendon Press, 1988.
43. Brillson, LJ and Lu, YC. ZnO Schottky barriers and Ohmic contacts. *J Appl Phys* 2011; **109**: 121301.
44. Wang, ZL. Preface to the special section on piezotronics. *Adv Mater* 2012; **24**: 4630–1.
45. Muller, RS, Kamins, TI and Chan, M. *Device electronics for integrated circuits*, 3rd edn. Hoboken, NJ: Wiley, 2002.
46. Yang, Q, Wang, WH and Xu, S *et al.* Enhancing light emission of ZnO microwire-based diodes by piezo-phototronic effect. *Nano Lett* 2011; **11**: 4012–7.
47. Zhang, Y, Liu, Y and Wang, ZL. Fundamental theory of piezotronics. *Adv Mater* 2011; **23**: 3004–13.
48. Espinosa, HD, Bernal, RA and Minary-Jolandan, M. A review of mechanical and electromechanical properties of piezoelectric nanowires. *Adv Mater* 2012; **24**: 4656–75.
49. Crowell, CR and Sze, SM. Current transport in metal-semiconductor barriers. *Solid State Electron* 1966; **9**: 1035–48.
50. Sze, SM. *Physics of semiconductor devices*. 2nd edn, New York: Wiley, 1981.
51. Zhou, J, Gu, YD and Fei, P *et al.* Flexible piezotronic strain sensor. *Nano Lett* 2008; **8**: 3035–40.
52. Fei, P, Yeh, PH and Zhou, J *et al.* Piezoelectric potential gated field-effect transistor based on a free-standing ZnO wire. *Nano Lett* 2009; **9**: 3435–9.
53. Zhou, YS, Wang, K and Han, WH *et al.* Vertically aligned CdSe nanowire arrays for energy harvesting and piezotronic devices. *ACS Nano* 2012; **6**: 6478–82.
54. Wu, WZ, Wen, XN and Wang, ZL. Taxel-addressable matrix of vertical-nanowire piezotronic transistors for active and adaptive tactile imaging. *Science* 2013; **340**: 952–7.
55. Liu, WH, Lee, M and Ding, L *et al.* Piezopotential gated nanowire-nanotube hybrid field-effect transistor. *Nano Lett.* 2010; **10**: 3084–9.
56. Yu, RM, Wu, WZ and Ding, Y *et al.* Gan nanobelt-based strain-gated piezotronic logic devices and computation. *ACS Nano* 2013.
57. Wang, ZL. Piezopotential gated nanowire devices: Piezotronics and piezo-phototronics. *Nano Today* 2010; **5**: 540–52.
58. Wang, ZL. Toward self-powered sensor networks. *Nano Today* 2010; **5**: 512–4.
59. Song, JH, Zhang, Y and Xu, C *et al.* Polar charges induced electric hysteresis of ZnO nano/microwire for fast data storage. *Nano Lett* 2011; **11**: 2829–34.

60. Linn, E, Rosezin, R and Kugeler, C *et al.* Complementary resistive switches for passive nanocrossbar memories. *Nat Mater* 2010; **9**: 403–6.
61. Takei, K, Takahashi, T and Ho, JC *et al.* Nanowire active-matrix circuitry for low-voltage macroscale artificial skin. *Nat Mater* 2010; **9**: 821–6.
62. Someya, T, Sekitani, T and Iba, S *et al.* A large-area, flexible pressure sensor matrix with organic field-effect transistors for artificial skin applications. *P Natl Acad Sci USA* 2004; **101**: 9966–70.
63. Mannsfeld, SCB, Tee, BCK and Stoltenberg, RM *et al.* Highly sensitive flexible pressure sensors with microstructured rubber dielectric layers. *Nat Mater* 2010; **9**: 859–64.
64. Wei, YG, Wu, WZ and Guo, R *et al.* Wafer-scale high-throughput ordered growth of vertically aligned ZnO nanowire arrays. *Nano Lett* 2010; **10**: 3414–9.
65. Huang, Y, Duan, XF and Wei, QQ *et al.* Directed assembly of one-dimensional nanostructures into functional networks. *Science* 2001; **291**: 630–3.
66. Wallentin, J, Anttu, N and Asoli, D *et al.* INP nanowire array solar cells achieving 13.8% efficiency by exceeding the ray optics limit. *Science* 2013; **339**: 1057–60.
67. Yuan, DJ, Guo, R and Wei, YG *et al.* Heteroepitaxial patterned growth of vertically aligned and periodically distributed ZnO nanowires on GaN using laser interference ablation. *Adv Funct Mater* 2010; **20**: 3484–9.
68. Wen, XN, Wu, WZ and Ding, Y *et al.* Seedless synthesis of patterned ZnO nanowire arrays on metal thin films (Au, Ag, Cu, Sn) and their application for flexible electromechanical sensing. *J Mater Chem* 2012; **22**: 9469–76.
69. Zhou, YS, Hinchet, R and Yang, Y *et al.* Nano-newton transverse force sensor using a vertical GaN nanowire based on the piezotronic effect. *Adv Mater* 2013; **25**: 883–8.
70. Yu, RM, Dong, L and Pan, CF *et al.* Piezotronic effect on the transport properties of GaN nanobelts for active flexible electronics. *Adv Mater* 2012; **24**: 3532–7.
71. Wu, JM, Chen, CY and Zhang, Y *et al.* Ultrahigh sensitive piezotronic strain sensors based on a $ZnSnO_3$ nanowire/microwire. *ACS Nano* 2012; **6**: 4369–74.
72. Dong, L, Niu, SM and Pan, CF *et al.* Piezo-phototronic effect of CdSe nanowires. *Adv Mater* 2012; **24**: 5470–5.
73. Wen, XN, Wu, WZ and Ding, Y *et al.* Piezotronic effect in flexible thin-film based devices. *Adv Mater* 2013; **25**: 3371–9.
74. Pan, CF, Yu, RM and Niu, SM *et al.* Piezotronic effect on the sensitivity and signal level of Schottky contacted proactive micro/nanowire nanosensors. *ACS Nano* 2013; **7**: 1803–10.
75. Yu, RM, Pan, CF and Wang, ZL. High performance of ZnO nanowire protein sensors enhanced by the piezotronic effect. *Energ Environ Sci* 2013; **6**: 494–9.
76. Han, WH, Zhou, YS and Zhang, Y *et al.* Strain-gated piezotronic transistors based on vertical ZnO nanowires. *ACS Nano* 2012; **6**: 3760–6.
77. Zhang, Y, Yan, XQ and Yang, Y *et al.* Scanning probe study on the piezotronic effect in ZnO nanomaterials and nanodevices. *Adv Mater* 2012; **24**: 4647–55.
78. Yang, Q, Liu, Y and Pan, CF *et al.* Largely enhanced efficiency in ZnO nanowire/p-polymer hybridized inorganic/organic ultraviolet light-emitting diode by piezo-phototronic effect. *Nano Lett* 2013; **13**: 607–13.
79. Zhang, F, Ding, Y and Zhang, Y *et al.* Piezo-phototronic effect enhanced visible and ultraviolet photodetection using a ZnO-CdS core-shell micro/nanowire. *ACS Nano* 2012; **6**: 9229–36.
80. Hu, YF, Zhang, Y and Lin, L *et al.* Piezo-phototronic effect on electroluminescence properties of p-type GaN thin films. *Nano Lett* 2012; **12**: 3851–6.
81. Pan, CF, Niu, SM and Ding, Y *et al.* Enhanced Cu_2S/CdS coaxial nanowire solar cells by piezo-phototronic effect. *Nano Lett* 2012; **12**: 3302–7.
82. Yang, Q, Guo, X and Wang, WH *et al.* Enhancing sensitivity of a single ZnO micro-/nanowire photodetector by piezo-phototronic effect. *ACS Nano* 2010; **4**: 6285–91.
83. Hu, YF, Zhang, Y and Chang, YL *et al.* Optimizing the power output of a ZnO photocell by piezopotential. *ACS Nano* 2010; **4**: 4220–4.
84. Zhang, Y, Yang, Y and Wang, ZL. Piezo-phototronics effect on nano/microwire solar cells. *Energ Environ Sci* 2012; **5**: 6850–6.
85. Liu, Y, Yang, Q and Zhang, Y *et al.* Nanowire piezo-phototronic photodetector: theory and experimental design. *Adv Mater* 2012; **24**: 1410–7.
86. Zhang, Y and Wang, ZL. Theory of piezo-phototronics for light-emitting diodes. *Adv Mater* 2012; **24**: 4712–8.
87. Yang, Y, Guo, WX and Zhang, Y *et al.* Piezotronic effect on the output voltage of P_3HT/ZnO micro/nanowire heterojunction solar cells. *Nano Lett* 2011; **11**: 4812–7.
88. Shi, J, Zhao, P and Wang, XD. Piezoelectric-polarization-enhanced photovoltaic performance in depleted-heterojunction quantum-dot solar cells. *Adv Mater* 2013; **25**: 916–21.
89. Konenkamp, R, Word, RC and Godinez, M. Ultraviolet electroluminescence from ZnO/polymer heterojunction light-emitting diodes. *Nano Lett* 2005; **5**: 2005–8.
90. Sun, XW, Huang, JZ and Wang, JX *et al.* A ZnO nanorod inorganic/organic heterostructure light-emitting diode emitting at 342 nm. *Nano Lett* 2008; **8**: 1219–23.
91. Xu, SG, Guo, WH and Du, SW *et al.* Piezotronic effects on the optical properties of ZnO nanowires. *Nano Lett* 2012; **12**: 5802–7.
92. Xue, XY, Wang, SH and Guo, WX *et al.* Hybridizing energy conversion and storage in a mechanical-to-electrochemical process for self-charging power cell. *Nano Lett* 2012; **12**: 5048–54.
93. Starr, MB, Shi, J and Wang, XD. Piezopotential-driven redox reactions at the surface of piezoelectric materials. *Angew Chem Int Edit* 2012; **51**: 5962–6.
94. Hou, YD, Abrams, BL and Vesborg, PCK *et al.* Bioinspired molecular co-catalysts bonded to a silicon photocathode for solar hydrogen evolution. *Nat Mater* 2011; **10**: 434–8.
95. Chen, XB, Liu, L and Yu, PY *et al.* Increasing solar absorption for photocatalysis with black hydrogenated titanium dioxide nanocrystals. *Science* 2011; **331**: 746–50.
96. Starr, MB and Wang, XD. Fundamental analysis of piezocatalysis process on the surfaces of strained piezoelectric materials. *Sci Rep* 2013; **3**: 2160.
97. Chen, XB, Shen, SH and Guo, LJ *et al.* Semiconductor-based photocatalytic hydrogen generation. *Chem Rev* 2010; **110**: 6503–70.
98. Liu, J, Cao, GZ and Yang, ZG *et al.* Oriented nanostructures for energy conversion and storage. *ChemSusChem* 2008; **1**: 676–97.
99. Yin, WJ, Tang, HW and Wei, SH *et al.* Band structure engineering of semiconductors for enhanced photoelectrochemical water splitting: the case of TiO_2. *Phys Rev B* 2010, 82.
100. Lewis, NS. Chemical control of charge transfer and recombination at semiconductor photoelectrode surfaces. *Inorg Chem* 2005; **44**: 6900–11.
101. Shi, J, Starr, MB and Xiang, H *et al.* Interface engineering by piezoelectric potential in ZnO-based photoelectrochemical anode. *Nano Lett* 2011; **11**: 5587–93.
102. Shi, J, Starr, MB and Wang, XD. Band structure engineering at heterojunction interfaces via the piezotronic effect. *Adv Mater* 2012; **24**: 4683–91.
103. Arden, W, Brillouët, M and Cogez, P *et al.* 'More-than-moore', white paper. *ITRS* 2010.